Order Number 9334924

On the dynamics of vortex propagation and associated asymmetric gyres

Li, Xiaofan, Ph.D.

University of Hawaii, 1993

U·M·I
300 N. Zeeb Rd.
Ann Arbor, MI 48106

ON THE DYNAMICS OF VORTEX PROPAGATION AND ASSOCIATED ASYMMETRIC GYRES

A DISSERTATION SUBMITTED TO THE GRADUATE DIVISION OF THE UNIVERSITY OF HAWAII IN PARTIAL FULFILLMENT OF THE REQUIREMENTS FOR THE DEGREE OF

DOCTOR OF PHILOSOPHY

IN

METEOROLOGY

AUGUST 1993

by

Xiaofan Li

Dissertation Committee:

Bin Wang, Chairperson
Gary M. Barnes
Dennis W. Moore
Thomas A. Schroeder
Duane E. Stevens

ACKNOWLEDGEMENTS

I am deeply indebted to my dissertation supervisor, Professor B. Wang, for his patience, encouragement and excellent guidance during the course of dissertation research.

I wish to thank my committee members: Professors G. Barnes, D. W. Moore, T. A. Schroeder, and D. E. Stevens, for their valuable comments and suggestions. Thanks also go to Professors Yiming Xu and Liang Fei, Shanghai Typhoon Institute, P. R. China for their support, Professor T. N. Krishnamurti, Florida State University for allowing me to use FSU regional model, Dr. T. Li for his shallow-water model and helpful discussion and Mr. M. Simpson for his technical assistance in optimization of the numerical codes of FSU model.

Finally, I would like to thank my wife, Qin Dong, my daughter, Di, and my parents for their love, understanding and long-term support during the five-year study.

ABSTRACT

Dynamics of vortex propagation and associated asymmetric gyres for a vortex being embedded in a resting environment and environmental flows on a beta-plane is investigated with a FSU regional model and a shallow-water model.

In a quiescent environment vortices with different initial horizontal structures follow substantially different tracks, which are associated with the evolution of the beta effect-induced counter-rotating gyres (beta-gyres). The beta-gyres are characterized by intensity variation, azimuthal rotation and outward movement.

Kinetic energy for development of beta-gyres primarily comes from symmetric circulation through planetary vorticity advection process (beta-conversion). An analysis of the beta-conversion reveals that (1) beta-gyres develop only when an anticyclonic gyre is located to the east of the cyclonic vortex center in the Northern Hemisphere, and (2) the rate of asymmetric kinetic energy generation increases with increasing relative angular momentum of the symmetric circulation.

The counterclockwise rotation of inner beta-gyres which are located near the maximum wind radius is caused by the advection of beta-gyre vorticity by symmetric cyclonic flow. However, the clockwise rotation of outer beta-gyres which are located near the periphery of the cyclonic azimuthal wind is determined by concurrent intensification in mutual advection of the asymmetric and symmetric circulations and weakening in

the advection of Earth's vorticity by symmetric circulation. The outward movement of the outer beta-gyres is mainly caused by the advection of symmetric vorticity by beta-gyres relative to the vortex drifting velocity.

The presence of environmental flows may change the intensity and orientation of asymmetric gyres whose flow over the vortex center advects symmetric vorticity and determine vortex propagation. The kinetic energy exchange between environmental flow and gyres is a key process responsible for the intensity difference of gyres between constant anticyclonic- and cyclonic-shear cases. The kinetic energy conversion from the environmental flow to gyres results in stronger gyres in constant anticyclonic-shear case, while that from the gyres to environmental flow causes weaker gyres in constant cyclonic-shear case.

For parabolic-jet cases in which environmental absolute vorticity gradient is zero or 2β, the small and larger rates of kinetic energy conversion from symmetric flow to gyres create, respectively, initial stronger and weaker gyres in the former and latter cases. The kinetic energy conversion between environmental and symmetric flows is a key process for the intensity evolution of gyres. The environmental flow feeds energy to symmetric flow in the former case causing dramatic development of symmetric vortex. As a result, the rate of asymmetric kinetic energy generation becomes larger causing stronger development of the gyres.

TABLE OF CONTENTS

LIST OF TABLES

LIST OF FIGURES

LIST OF SYMBOLS

σ	dimensionless vertical coordinate ($\sigma=p/p_s$)
p	pressure
p_s	pressure at the earth's surface
V	total horizontal wind vector
u,v	zonal and meridional components of wind vector
t	time
$\dot{\sigma}$	vertical velocity in sigma coordinate
f	Coriolis parameter
β	meridional gradient of Coriolis parameter
a	earth's radius
g	gravity
z	height
ϕ	geopotential
R	specific gas constant for dry air
T	temperature
F_x, F_y	zonal and meridional components of friction
F	horizontal friction vector
x,y	x- and y-coordinates
κ	$=R/C_p$
C_p	specific heat for dry air at constant pressure
D_T	diabatic heating (cooling) per unit mass
Φ	latitude
ζ	vertical component of relative vorticity

δ	horizonal divergence
ω	vertical velocity in pressure coordinate
ψ	stream function
χ	velocity potential
$\mathbf{k}$	vertical unit vector
r	radial distance from vortex center
λ	azimuthal angle from due north counterclockwise

CHAPTER ONE

INTRODUCTION

Tropical cyclone motion is persistently different from an environmental steering (e.g., George and Gray 1976; Chan and Gray 1982; Carr and Elsberry 1989). The difference (referred to as a propagation) results from the interactions between the tropical cyclone circulation and the environment. Physical processes that may contribute to the propagation include: an interaction of the tropical cyclone with the planetary vorticity gradient (Chan and Williams 1987; Fiorino and Elsberry 1989a), a response to spatially-varying environmental flow (DeMaria 1985; Ulrich and Smith 1991; Williams and Chan 1992; Shapiro 1992), an interaction of the moving tropical cyclone with the boundary layer (Shapiro 1983), and a response to convective asymmetries (Jones 1986).

Theoretically, an adiabatic motion of tropical cyclone is determined by an advection by an environmental steering and an advection by a uniform flow of counter-rotating gyres near the vortex center, which are generated by the advection of environmental absolute potential vorticity by symmetric vortex flows. This dissertation research is to investigate the dynamics of vortex propagation and associated asymmetric gyres for a vortex which is embedded in a resting environment and in meridionally-varying environmental flows.

Beta-drift and associated beta-gyres

The movement of a vortex embedded in a quiescent environment on a beta-plane (the beta-drift) is explained by vorticity dynamics. Adem (1956) first worked out asymptotic solution for a non-divergent barotropic vorticity equation and found a beta effect-induced asymmetric circulation which drives a cyclonic vortex first westward and then poleward. Holland (1983) argued that the advection of planetary vorticity by cyclonic symmetric azimuthal flow creates asymmetric vorticity field, which is featured by a pair of counter-rotating gyres, counterclockwise to the west of the vortex center and clockwise to the east in the Northern Hemisphere. This pair of gyres are referred to as beta-gyres. Fiorino and Elsberry (1989a) further found that the two largest terms in non-divergent barotropic vorticity equation, the advection of asymmetric vorticity by the symmetric flow and the advection of planetary vorticity by the symmetric flow, approximately cancel each other, thus, the beta-drift can be predicted by a uniform flow of beta-gyres near the vortex center which advects the symmetric vorticity. This uniform flow is referred to as ventilation flow. Therefore, a key to understanding the beta-drift is to explain the dynamics of the beta-gyres.

Rossby's (1948) pioneer study showed that northward drift of a rotating rigid-body is related to its relative angular

velocity. Adem (1956) found that the initial westward and subsequential northward drifts are, respectively, proportional to the radius and maximum azimuthal wind of the vortex. DeMaria (1985) noticed that vortex drift is much more sensitive to changes in its size than to changes in its intensity. On the other hand, Chan and Williams (1987) found that beta-drift speed depends almost linearly upon the inner circulation parameters: the maximum azimuthal wind and the radius of maximum wind. Fiorino and Elsberry (1989a) partitioned the initial symmetric vortex wind profile into inner and outer flows, and found that the intensity of the inner flows has little effect, while the strength of the outer flows has a significant effect on the beta-drift. Wang and Li (1992) reconciled the previous results in terms of mean relative angular momentum (MRAM). Their numerical experiments revealed that the northward component and the total speed of the beta-drift averaged from 12 to 36 hours after initialization are proportional to the square root of the magnitude of MRAM of the initial symmetric vortex. Since MRAM is a quadratic function of radial distance from the vortex center, it follows that the outer flows contribute more to MRAM than the inner flows do, so that the beta-drift is more sensitive to the changes in the outer flows. An objective of this research is to explain the relationship between vortex structure and beta-drift speed. Since the beta-drift speed is determined by the strength of beta-gyres (Fiorino and Elsberry

1989a), the dynamic processes responsible for development of beta-gyres will be investigated.

Beta-drift and associated beta-gyres are found to be quasi-steady in the most previous studies. Another objective of this research is to demonstrate that vortices with differing horizontal structures follow substantially different tracks. The tracks are associated with the evolution of beta-gyres. Thus the azimuthal and radial movement of beta-gyres, which results in the unsteady tracks, will be examined.

Effect of spatially-varying environmental flows on vortex propagation

A barotropic symmetric vortex embedded in a uniform environmental flow on an f-plane moves exactly with the uniform flow (Adem and Lezama 1960). However, when a barotropic symmetric vortex is embedded in a spatially-varying environmental flow, mainly constant-shear or parabolic-jet flow, the propagation on a beta-plane is significantly different from that in the case without environmental flow, indicating the effect of environmental flows on the vortex propagation (e.g., Ulrich and Smith 1991; Williams and Chan 1992).

Sasaki (1955) and Kasahara (1957) showed that environmental relative vorticity gradient causes a cyclonic

vortex to move in a direction 90° to the left to the direction of the vorticity gradient. DeMaria (1985) further revealed that environmental absolute vorticity gradient causes a cyclonic vortex to drift relative to the flow with a component in the direction of the gradient and a component 90° to the left of the gradient. To isolate the effect of environmental relative vorticity gradient on vortex motion, Ulrich and Smith (1991) designed an experiment on an f-plane in which environmental flow has a relative vorticity gradient that equals β and found in the Northern Hemisphere much smaller northward displacement of a cyclonic vortex compared to that in the case with a quiescent environment on a beta-plane. Williams and Chan (1992) revealed that contribution from planetary vorticity gradient to motion is more important than the contribution from meridional gradient of environmental relative vorticity because the latter contains the advection of symmetric vorticity by the environmental flow that partially cancels the effect of the relative vorticity gradient on the motion. They further made two parabolic-jet experiments on a beta-plane in which environmental absolute vorticity gradient is zero or 2β and revealed that the vortex propagation is slower first and then becomes faster in the former case than that in the latter case.

Ulrich and Smith (1991), and Smith (1991) examined the roles of constant-shear environmental flows in vortex motion using a non-divergent barotropic model. They found that

although constant-shear flows are zonal, the northward component of motion of a cyclonic vortex in constant anticyclonic-shear case is significantly larger than that in constant cyclonic-shear case. Williams and Chan (1992) conducted experiments similar to those done by Ulrich and Smith (1991). After the advection by the environmental flow is subtracted, they found that the tracks in cases with constant cyclonic- and anticyclonic-shear flows have the same orientation as the track in the case with no environmental flow. The constant cyclonic-shear track is about the same length as the track with no environmental flow, but the constant anticyclonic-shear track is significantly longer.

The propagation is in accord with the evolution of asymmetric gyres for both constant-shear and parabolic-jet cases (Williams and Chan 1992). Thus another objective of this research is to elucidate what causes the difference in intensity of the gyres between constant anticyclonic- and cyclonic-shear cases and what controls the different intensity evolution of the gyres in the parabolic-jet cases.

The major objectives of this study are 1) to identify the dynamic processes responsible for unsteady beta-gyres and beta-drift, and 2) to reveal the dynamic mechanisms responsible for vortex propagation in the presence of spatially-varying environmental flows.

To isolate the essential dynamic mechanisms in vortex propagation, the dry version of a Florida State University regional model and a shallow-water model, which are briefly described in chapter two, are used in this study. Objective 1 and 2 will be discussed in chapter three and chapter four, respectively. Chapter five gives conclusions.

CHAPTER TWO

NUMERICAL MODELS

2.1 The dry version of Florida State University Regional Model

The Florida State University Region Model (Krishnamurti et al. 1990) is used in chapter three. This is a primitive equation model on sigma coordinates in which

$$\sigma = \frac{p}{p_s}, \tag{2.1}$$

where p is the pressure and p_s is the pressure at the earth's surface.

The governing equations for a Lagrangian formulation are written as follows:

$$\frac{Du}{Dt} = -\dot{\sigma}\frac{\partial u}{\partial \sigma} + v\left(f + \frac{u}{a}\tan\Phi\right) - g\frac{\partial z}{\partial x} - RT\frac{\partial \ln P_s}{\partial x} + F_x, \tag{2.2a}$$

$$\frac{Dv}{Dt} = -\dot{\sigma}\frac{\partial v}{\partial \sigma} + u\left(f + \frac{u}{a}\tan\Phi\right) - g\frac{\partial z}{\partial y} - RT\frac{\partial \ln P_s}{\partial y} + F_y, \tag{2.2b}$$

$$\frac{DT}{Dt} = -\dot{\sigma}\frac{\partial T}{\partial \sigma} + \kappa T\left(\frac{\dot{\sigma}}{\sigma} + \frac{\partial \ln P_s}{Dt}\right) + \frac{D_T}{C_p}, \tag{2.2c}$$

$$\frac{D\ln P_s}{Dt} = -\frac{\partial \dot{\sigma}}{\partial \sigma} - \nabla\cdot\mathbf{v}, \tag{2.2d}$$

$$\frac{\partial z}{\partial \sigma} = -\frac{RT}{g\sigma}, \tag{2.2e}$$

where $\frac{D}{Dt} = \frac{\partial}{\partial t} + u\frac{\partial}{\partial x} + v\frac{\partial}{\partial y}$.

Equations (2.2a) and (2.2b) are the momentum equations in the x- and y-directions, respectively. Equation (2.2c) is the thermodynamic equation. The mass continuity equation is (2.2d) and the hydrostatic equation is (2.2e).

Semi-Lagrangian and semi-implicit schemes were applied to an Arakawa C-type staggered grid (Krishnamurti 1962, 1969; Robert et al. 1972; Arakawa and Lamb 1976). The detailed results of sensitivity tests about the friction coefficient, horizontal and vertical resolution, and domain size are given by Wang and Li (1992). For the dry version of the model, diabatic heating term D_T in Eq. (2.2c) is set to zero.

2.2 Shallow-water model

As noticed by McCalpin (1988), the semi-Lagrangian advection scheme produces strong inherent dissipation. In the dry version of FSU regional model, the intensity of vortex is significantly reduced as time proceeds. To make extended-range time integration, a shallow-water model developed by Li and Zhu (1991) is used.

$$\frac{\partial}{\partial t}(\phi \mathbf{V}) + \nabla\cdot(\phi \mathbf{V}\mathbf{V}) + \phi f \mathbf{k}\times\mathbf{V} = -\phi\nabla\phi, \qquad (2.3a)$$

$$\frac{\partial}{\partial t}\phi + \nabla\cdot(\phi \mathbf{V}) = 0, \qquad (2.3b)$$

where $\mathbf{V}$ and ϕ are the total wind the geopotential, and f is the Coriolis parameter.

The shallow-water model was used to study the effect of meridionally-varying environmental flows on vortex propagation. The initial environmental flows were chosen to be steady solutions of the (2.3). Two versions of model are designed. Model A which allows environmental flow changing with time is (2.3). Model B fixes environmental flow during integration. The total wind is decomposed into a vortex circulation ($\mathbf{V}_v$) and a time-independent environmental flow ($\mathbf{V}_c$) with meridional variation

$$\mathbf{V} = \mathbf{V}_v + \mathbf{V}_c. \tag{2.4a}$$

The geopotential is the sum of a vortex part (ϕ_v) and an environmental part (ϕ_c)

$$\phi = \phi_v + \phi_c. \tag{2.4b}$$

Substituting (2.4) into (2.3) yields

$$\frac{\partial}{\partial t}(\phi_v \mathbf{V}_v) + \nabla\cdot(\phi_v \mathbf{V}_v \mathbf{V}_v) + \phi_v f \mathbf{k}\times\mathbf{V}_v = -\phi_v \nabla\phi_v - \nabla\cdot(\phi_v \mathbf{V}_v \mathbf{V}_c)$$

$$- \mathbf{V}_v \nabla\cdot(\phi_c \mathbf{V}_v) - \phi_v \mathbf{V}_v \cdot \nabla \mathbf{V}_c, \tag{2.5a}$$

$$\frac{\partial}{\partial t}\phi_v + \nabla\cdot(\phi_v \mathbf{V}_v) = -\nabla\cdot(\phi_c \mathbf{V}_v) - \nabla\cdot(\phi_v \mathbf{V}_c), \qquad (2.5b)$$

Sensitivity tests reveal that the maximum difference of vortex centers between model A and model B is less than 2 km in a 72-hour integration for constant-shear case C_2 whereas less than 10 km in a 108-hour integration for parabolic-jet case D_1 (see sections two and three in chapter four), indicating that the temporal variation of the chosen environmental flow has no significant effect on vortex propagation. For convenience, model B is adopted in chapter four.

2.3 Initial field and definition of vortex center

The wind field is first given for the initial vortex. The initial geopotential height field inside the vortex is computed using the gradient wind relationship. Outside the vortex a typical vertical structure of geopotential height for a tropical environment in hurricane season (Jordan 1958) is assumed in the FSU model (Wang and Li 1992) and mean geopotential of 2.5×10^4 m^2s^{-2} is assumed in the shallow-water model. Initial environmental flow is geostrophic.

Surface pressure in the FSU model and geopotential in the shallow-water model are directly obtained. Therefore, the

minimum surface pressure and minimum geopotential are defined as the vortex center in the FSU and the shallow-water models, respectively.

2.4 separation of the symmetric/asymmetric circulation

To partition the vortex circulation into symmetric and asymmetric components, the following procedures are implemented: The model solution is interpolated into a fine mesh of 20 km using a cubic spline method (de Boor 1978). Then the fine mesh in Cartesian coordinates is transformed into cylindrical coordinates moving with the vortex using a quadratic function expansion. The symmetric component is obtained by averaging in azimuthal direction, and the asymmetric component is defined as the difference between the total circulation and the symmetric component. Finally, the values in cylindrical coordinates are transformed back to Cartesian coordinates.

CHAPTER THREE

DYNAMICS OF UNSTEADY BETA-GYRES AND BETA-DRIFT

Dynamics of unsteady beta-gyres and beta-drift is investigated in this chapter. It focuses on two aspects: development of beta-gyres, and the azimuthal and radial movement of beta-gyres. In section 3.1, necessary and favorable conditions for development of beta-gyres is discussed. In section 3.2, dominant radial modes are analyzed for the circulation and energetics. The evolution of the beta-gyres associated with the beta-drift is analyzed in section 3.3. The dynamic processes controlling the azimuthal and radial movement of the beta-gyres are examined in section 3.4. The major findings are summarized in the last section.

3.1 Development of the beta-gyres

3.1.1 Two numerical experiments

A 6-level, dry version of the FSU regional model developed by Krishnamurti et al. (1990) was used. Based on the sensitivity tests made by Wang and Li (1992), a horizontal domain 5520×3920 km^2 is chosen with a square mesh of 80 km. Sponge layers are used to furnish lateral boundary conditions. Integrations are all carried out for 48 hours.

Initial vortices are axially symmetric and pure

rotational. The azimuthal wind profile v_λ is expressed as

$$v_\lambda(r,p)=v_r(r)v_p(p), \tag{3.1}$$

where r and p are the radial distance from the vortex center and pressure, respectively, v_r and v_p are, respectively, the radial and vertical distributions of v_λ.

To examine the beta-drift and associated beta-gyres for vortices with different horizontal structures, two types of cyclonic vortices were designed. In the first case, the case S, the initial vortex has a strong cyclonic flow inside 750 km radius and a positive total relative regular momentum (TRAM). Its azimuthal wind profile shown in Fig. 1a is given by

$$v_r(r)=\begin{cases} V_m\dfrac{r}{r_m}\{\exp[1-(\dfrac{r}{r_m})]-\dfrac{|r-r_m|}{|R_o-r_m|}\exp[1-(\dfrac{R_o}{r_m})]\} & r\le R_o, \\ 0 & r>R_o, \end{cases} \tag{3.2a}$$

where V_m=30 ms^{-1} is the maximum wind, r_m=200 km is the radius of maximum wind, R_o=750 km is the vortex radius.

In the second case, the case W, the initial vortex consists of cyclonic flows inside the radius of 600 km and weak anticyclonic flows in the annulus between 600 km and 1000 km, so that the TRAM of the vortex vanishes (Fig. 1a). The azimuthal wind profile is similar to that used by Willoughby (1988):

$$v_r(r)=\begin{cases} 0.9v_m r/r_1, & 0\le r\le r_1, \\ v_m[1-\eta_A(r_m-r)^2+\eta_C(r_m-r)^3], & r_1<r\le r_m, \\ v_m[1-\eta_A(r_m-r)^2+\eta_B(r_m-r)^3], & r_m<r\le r_2, \\ v_m[(v_B+0.1)(\dfrac{r_3-r}{r_3-r_2})^2-0.1], & r_2<r\le R_o. \end{cases} \quad (3.2b)$$

Here, v_m=30 ms^{-1}, r_1=180 km, r_m=200 km, r_2=300 km, r_3=800 km, R_o=1000 km, η_A, η_B, η_C and v_B are determined by the continuity conditions of the wind profile at points r_1 and r_2, and the first order of radial differential at points r_2, and the condition v_λ(600 km)=0.

The vertical wind profile in both case S and case W is shown by the thick solid curve in Fig. 1b.

Figure 2 displays vortex tracks during 48-hour integrations for the two cases. The vortex in case S moves northwestward persistently within the entire integration period, while the vortex in case W moves northwestward during the first 30 hours, and then recurves northeastward from hour 30 to 48. Notice that the beta-drift speed in case S is much larger than that in case W. The primary questions are: How does vortex structure control the beta-drift speed? What are necessary and favorable conditions for beta-gyres to develop? The next subsections will offer the answers.

3.1.2 Kinetic energy equations

A set of energy equations was derived for diagnostic analysis. Total velocity is partitioned into rotational ($\mathbf{V}_\psi$) and divergent ($\mathbf{V}_\chi$) components:

$$\mathbf{V} = \mathbf{V}_\psi + \mathbf{V}_\chi, \qquad \mathbf{V}_\psi = \mathbf{k}\times\nabla\psi, \qquad \mathbf{V}_\chi = \nabla\chi, \tag{3.3a}$$

where ψ and χ are stream function and velocity potential, respectively.

Both rotational and divergent winds can be advantageously decomposed into symmetric and asymmetric components, i.e.,

$$\psi=\psi_s+\psi_a, \qquad \chi=\chi_s+\chi_a, \tag{3.3b}$$

where subscripts "s" and "a" represent the symmetric and asymmetric component, respectively.

The vorticity and divergence equations, respectively, are,

$$\frac{\partial\zeta}{\partial t} = -\mathbf{V}\cdot\nabla(\zeta+f) - \omega\frac{\partial\zeta}{\partial p} - (\zeta+f)\delta - \mathbf{k}\cdot\nabla\omega\times\frac{\partial\mathbf{V}}{\partial p} + \mathbf{k}\cdot\nabla\times\mathbf{F} \tag{3.4a}$$

$$\frac{\partial\delta}{\partial t} = -\mathbf{V}\cdot\nabla\delta - \omega\frac{\partial\delta}{\partial p} - (\zeta+f)\delta - \nabla\omega\cdot\frac{\partial\mathbf{V}}{\partial p} + \delta^2 + J(u,v)$$
$$-(\mathbf{k}\times\mathbf{V})\cdot\nabla f + f\zeta - \nabla^2\phi + \nabla\cdot\mathbf{F} \tag{3.4b}$$

where $\mathbf{V}$ and ω represent total horizontal wind and vertical pressure velocity, respectively; ζ, and δ are the vertical component of relative vorticity and horizontal divergence respectively; $J(a,b)=(\partial a/\partial x)(\partial b/\partial y)-(\partial b/\partial x)(\partial a/\partial y)$; $\mathbf{F}$ denotes friction.

The total kinetic energy components for symmetric and

asymmetric rotational and divergent flows are defined as follows:

$$K_{\psi s} = < \frac{\nabla\psi_s \cdot \nabla\psi_s}{2} >, \tag{3.5a}$$

$$K_{\psi a} = < \frac{\nabla\psi_a \cdot \nabla\psi_a}{2} >, \tag{3.5b}$$

$$K_{\chi s} = < \frac{\nabla\chi_s \cdot \nabla\chi_s}{2} >, \tag{3.5c}$$

$$K_{\chi a} = < \frac{\nabla\chi_a \cdot \nabla\chi_a}{2} >, \tag{3.5d}$$

where the angle bracket implies a volume integration:

$$<(\quad)> = \frac{1}{g}\int_{Pt}^{Pb} dp \int_0^{ro} r dr \int_0^{2\pi} (\quad) d\lambda, \tag{3.6}$$

where p_t and p_b are the pressures at the upper and lower boundaries of the model, respectively, and r_o is the radius of the integrated domain and r_o=1200 km.

A set of kinetic energy equations was derived by multiplying the vorticity equation by ψ_s and ψ_a and the divergence equation by χ_s and χ_a respectively, and applying the integration defined by (3.6) on these equations:

$$\frac{\partial}{\partial t}K_{\psi s} = F_{\psi s} + (K_{\chi s}, K_{\psi s}) + (K_{\chi a}, K_{\psi s}) + (K_{\psi a}, K_{\psi s}) + D_{\psi s}, \tag{3.7a}$$

$$\frac{\partial}{\partial t}K_{\psi a} = F_{\psi a} + (K_{\chi s},K_{\psi a}) + (K_{\chi a},K_{\psi a}) - (K_{\psi a},K_{\psi s}) + D_{\psi a}, \quad (3.7b)$$

$$\frac{\partial}{\partial t}K_{\chi s} = F_{\chi s} + (K_{\chi a},K_{\chi s}) - (K_{\chi s},K_{\psi s}) - (K_{\chi s},K_{\psi a})$$

$$+ (P+I,K_{\chi s}) + D_{\chi s}, \quad (3.7c)$$

$$\frac{\partial}{\partial t}K_{\chi a} = F_{\chi a} - (K_{\chi a},K_{\chi s}) - (K_{\chi a},K_{\psi s}) - (K_{\chi a},K_{\psi a})$$

$$+ (P+I,K_{\chi a}) + D_{\chi a}, \quad (3.7d)$$

where P+I is total potential energy, $F_{\psi s}$, $F_{\psi a}$, $F_{\chi s}$, and $F_{\chi a}$ are the energy fluxes due to radial flows evaluated at the outer radial boundary of the integration domain, and $D_{\psi s}$, $D_{\psi a}$, $D_{\chi s}$, and $D_{\chi a}$ are the dissipation terms. Notation (A,B) means that energy is converted from A to B.

The kinetic energy conversion terms in the energy equations (3.7) are defined as follows:

$$(K_{\chi s},K_{\psi s}) = <(\mathbf{V}\cdot\nabla\mathbf{V}_{\psi s})\cdot\mathbf{V}_{\chi s}> + <\omega\mathbf{V}_{\chi s}\cdot\frac{\partial\mathbf{V}_{\psi s}}{\partial p}> - <f\nabla\chi_s\cdot\nabla\psi_s>, \quad (3.8a)$$

$$(K_{\chi a},K_{\psi s}) = <(\mathbf{V}\cdot\nabla\mathbf{V}_{\psi s})\cdot\mathbf{V}_{\chi a}> + <\omega\mathbf{V}_{\chi a}\cdot\frac{\partial\mathbf{V}_{\psi s}}{\partial p}> - <f\nabla\chi_a\cdot\nabla\psi_s>, \quad (3.8b)$$

$$(K_{\psi a},K_{\psi s}) = <(\mathbf{V}\cdot\nabla\mathbf{V}_{\psi s})\cdot\mathbf{V}_{\psi a}> + <\omega\mathbf{V}_{\psi a}\cdot\frac{\partial\mathbf{V}_{\psi s}}{\partial p}> - <f\mathbf{k}\cdot\nabla\psi_a\times\nabla\psi_s>, \quad (3.8c)$$

$$(K_{\chi s},K_{\psi a}) = <(\mathbf{V}\cdot\nabla\mathbf{V}_{\psi a})\cdot\mathbf{V}_{\chi s}> + <\omega\mathbf{V}_{\chi s}\cdot\frac{\partial\mathbf{V}_{\psi a}}{\partial p}> - <f\nabla\chi_s\cdot\nabla\psi_a>, \quad (3.8d)$$

$$(K_{\chi a}, K_{\psi a}) = <(\mathbf{V}\cdot\nabla\mathbf{V}_{\psi a})\cdot\mathbf{V}_{\chi a}> + <\omega\mathbf{V}_{\chi a}\cdot\frac{\partial\mathbf{V}_{\psi a}}{\partial p}> - <f\nabla\chi_a\cdot\nabla\psi_a>, \quad (3.8e)$$

$$(K_{\chi a}, K_{\chi s}) = <(\mathbf{V}\cdot\nabla\mathbf{V}_{\chi s})\cdot\mathbf{V}_{\chi a}> + <\omega\mathbf{V}_{\chi a}\cdot\frac{\partial\mathbf{V}_{\chi s}}{\partial p}> - <f\mathbf{k}\cdot\nabla\chi_a\times\nabla\chi_s>, \quad (3.8f)$$

$$(P+I, K_{\chi s}) = -<\nabla\chi_s\cdot\nabla\phi_s>, \quad (3.8g)$$

$$(P+I, K_{\chi a}) = -<\nabla\chi_a\cdot\nabla\phi_a>. \quad (3.8h)$$

For both cases, $K_{\chi s}$ and $K_{\chi a}$ are the orders of 10^{15} J, whereas $K_{\psi a}$ and $K_{\psi s}$ are, respectively, the orders of 10^{16} J and 10^{18} J. This indicates that the divergent flow is negligible.

As far as the asymmetric flow is concerned, only the rotational component, $K_{\psi a}$, needs to be considered. Table 1 reveals that for each case the kinetic energy for the development of asymmetric circulation is primarily converted from symmetric circulation. Asymmetric circulation develops by extracting the kinetic energy from the symmetric circulation against the dissipation and the outward radiation of energy. Notice also that the flux term $F_{\psi a}$ is one order of magnitude smaller than the conversion from $K_{\psi s}$ to $K_{\psi a}$ in case S while it is three orders of magnitude smaller in case W. This suggests that for a vortex with a zero TRAM, the radiation of kinetic energy is negligible. On the other hand, for a vortex which has a positive TRAM, there is an appreciable kinetic energy leakage. The negative flux in case S means an outward energy dispersion due to Rossby wave radiation (McWilliams and Flirl 1979).

The rate of kinetic energy conversion from symmetric to asymmetric rotational flows, $(K_{\psi s}, K_{\psi a})$, can be expressed, from Eq. (3.8c), by

$$(K_{\psi s}, K_{\psi a}) = CT_1 + CT_2 + CT_3, \tag{3.9}$$

where

$$CT_1 = -\langle (\mathbf{V} \cdot \nabla \mathbf{V}_{\psi s}) \cdot \mathbf{V}_{\psi a} \rangle, \tag{3.9a}$$

$$CT_2 = -\langle \omega \mathbf{V}_{\psi a} \cdot \partial \mathbf{V}_{\psi s} / \partial p \rangle, \tag{3.9b}$$

$$CT_3 = \langle \beta r \cos\lambda \mathbf{k} \cdot (\nabla \psi_a \times \nabla \psi_s) \rangle. \tag{3.9c}$$

Terms CT_1 and CT_2 represent, respectively, the conversion due to nonlinear horizontal and vertical advection of symmetric circulation, and term CT_3 is due to the beta-effect. For convenience we refer CT_3 and CT_1 to as beta-conversion and nonlinear-conversion, respectively. Term CT_2 is two orders of magnitude smaller than CT_1 (Table 2). As noticed by Carr and Williams (1989), the nonlinear-conversion is determined by the covariance between the radial phase tilt of beta-gyres and the radial gradient of symmetric angular wind (defined as the azimuthal wind of symmetric vortex divided by the radial distance). The beta-conversion is determined by the beta-effect, and the vertical component of the vector product of the symmetric, and the asymmetric rotational flows.

As shown in Table 2, the major contribution to $(K_{\psi s}, K_{\psi a})$ for both cases is the beta-conversion, i.e., the meridional variation of Coriolis parameter plays a key role in transferring kinetic energy from the symmetric into the

asymmetric circulation. The importance of nonlinear-conversion CT_1, however, depends on the structure of the symmetric circulation. It is very small compared to CT_3 in case S whereas it has the same order of magnitude as CT_3 in case W. Further, Figures 3-5 show the vertical-radial distributions of the nonlinear conversion (CT_1), the beta-conversion (CT_3) and the conversion from $K_{\psi s}$ to $K_{\psi a}$ at hour 6 for the two cases.

In case S, the nonlinear-conversion has significant values only within 300 km radius. The positive area centered at 150 km radius and the negative area centered at 250 km radius almost cancel each other over the circular area within the radius of 1200 km so that total nonlinear-conversion is quite small (Fig. 3a). On the other hand, the maximum beta-conversion is within 400-500 km radius and at the lowest levels (Fig. 3b). The conversion from $K_{\psi s}$ to $K_{\psi a}$ shows almost the same pattern as the beta-conversion because it is dominated by the beta-conversion (Fig. 5a). In case W, the nonlinear-conversion has the similar pattern as the beta-conversion, but the former is weaker than the latter (Fig. 4) so that the beta-conversion dominates the conversion from $k_{\psi s}$ to $K_{\psi a}$ (Fig. 5b). The maximum positive center of both conversions is around 200-300 km radius and at the lower levels. In short, the maximum positive center of conversion from $K_{\psi s}$ to $K_{\psi a}$ locates abound 400-500 km radius in case S while around 200-300 km radius in case W, and the positive values extend to 700 km radius in case S but 500 km radius in case W.

3.1.3 Necessary and favorable conditions for the development of the beta-gyres

Since the beta-conversion is the major process by which the beta-gyres extract energy from symmetric circulation, the focus of theoretical analysis is on the beta-conversion in the following discussions. In cylindrical coordinates, the beta-conversion can be expressed as

$$CT_3 = -\beta\langle r\cos\lambda \frac{\partial\psi_a}{r\partial\lambda} \frac{\partial\psi_s}{\partial r}\rangle, \qquad (3.10)$$

where r is a radial distance from vortex center, and λ is an azimuthal angle measured counterclockwise from due north.

For simplicity, consider a cyclonic vortex and beta-gyres for which

$$\psi_s = R_s(r)Z_s(p) \qquad R_s,\ Z_s > 0, \qquad (3.11a)$$

$$\psi_a = R_a(r)Z_a(p)\cos(\alpha-\lambda) \qquad R_a,\ Z_a > 0, \qquad (3.11b)$$

where R_s and R_a are the amplitudes of the symmetric circulation and the beta-gyres, respectively; Z_s and Z_a are the vertical distribution of the symmetric circulation and the beta-gyres, respectively, and α is an azimuthal angle of the anticyclonic-gyre center measured counterclockwise from due north.

Substituting (3.11a,b) into (3.10) yields

$$CT_3=-\beta<Z_sZ_a\frac{\partial R_s}{\partial r}R_a\cos^2\lambda>\sin\alpha$$

$$=-[\frac{1}{g}\int_{p_t}^{p_b} Z_sZ_a dp][\beta\pi\sin\alpha\int_0^{r_o}\frac{\partial R_s}{\partial r}rR_a dr]. \qquad (3.12)$$

In an f-plane the beta-conversion vanishes so that symmetric vortex does not drift. In the presence of a meridional gradient of the Coriolis parameter, the following two inferences can be made.

(1) Necessary condition for the beta-gyres to develop is that an anticyclonic gyre is located to the east of the cyclonic vortex center in the Northern Hemisphere.

In order for $CT_3>0$, α in (3.12) should be within $(-\pi, 0)$. This indicates that in the Northern Hemisphere the anticyclonic gyre should be located to the east of the cyclonic vortex center in order for the kinetic energy to transfer from the symmetric circulation to the beta-gyres. Although the anticyclonic gyre rotates from the northeast to the southeast quadrants in numerical simulations (e.g., Fiorino and Elsberry 1989a), the pattern remains favorable for $CT_3>0$. Both cases satisfy the necessary condition for the development of the beta-gyres.

(2) The radial distribution of the beta-conversion depends on the radial distribution of the RAM or the symmetric vortex circulation.

In (3.12), the beta-conversion is proportional to the

covariance between the RAM of symmetric circulation and the amplitude of beta-gyres. Radial maximum of RAM appears around 400 km in case S whereas it is near 250 km in case W (Fig. 6a). The radial maximum of beta-gyres occurs around 500-800 km in case S whereas it is around 300 km in case W (Fig. 6b). Since the RAM in case S is radially symmetric about 400 km, the radial maximum of beta-gyres between 500 and 800 km results in the radial maximum of the beta-conversion around 400-500 km. The radial maximum of beta-gyres at 300 km and large values of the RAM around 250 km in case W contribute to the radial maximum of the beta-conversion around 200-300 km. Since the radial distribution of amplitude of beta-gyres is determined by the radial distribution of RAM of symmetric circulation (see next paragraph), the maximum generation of asymmetric kinetic energy approximately lies in the maximum of RAM. Therefore, the rate of beta-conversion is determined by the MRAM or the symmetric vortex structure. As MRAM increases, more asymmetric kinetic energy is generated resulting in stronger beta-gyres and a larger drift. This supports the empirical relationship between MRAM and beta-drift speed numerically established by Wang and Li (1992).

The asymmetric circulation is created by the beta-effect initially. Figs 7a,b show that at the first time step of the integration the asymmetric circulation in case S is much stronger than that in case W. The vortex carrying a large MRAM obviously creates a stronger and a larger initial asymmetric

circulation. The strong asymmetric circulation interacting with the stronger symmetric circulation will further promote more kinetic energy conversion from the symmetric to asymmetric circulation, making the vortex move at a higher speed in case S. Total speeds of the beta-drift are, respectively, 1.08 ms^{-1} and 0.51 ms^{-1} at hour 6 for cases S and W.

3.2 Radial modes associated with the beta-drift

Fiorino and Elsberry (1989b) applied a Fourier transform technique on an initial vortex wind profile to investigate the contributions to tropical cyclone motion by small, medium and large scales in the initial vortex. They found that the largest scales (>1500 km) determine the speed of motion, and medium ($500<\lambda\leq1500$ km) and small (≤500 km) scales have a significant effect on the direction of motion. Their results suggest that different radial modes play quite different roles in vortex motion. Last section also reveals that the difference in the asymmetric kinetic energy generation between case S and case W stems from the difference in the initial symmetric vortex circulation. To elaborate this point, this section examines the difference between case S and case W in dominant radial modes for the symmetric and asymmetric circulations and for the kinetic energy conversion. For the

vortex with a vertical wind profile as in cases S and W, the circulation at 625 mb is representative of a steering level (Wang and Li 1992). In a dry model, the circulation patterns at all vertical levels are very similar. Therefore, the radial modes at 625 mb are analyzed.

The cylindrical coordinates moving with the vortex are established. The radial mode decomposition depends on the outer boundary conditions. The choice of outer boundary condition is not unique. First, it is assumed that the radial component of the vortex circulation vanishes at the outer boundary. Secondly, the choice of radial distance of outer boundary should make the highly-truncated expansion series converge quickly. Therefore, for both cases S and W, the radial distance of the outer radial boundary is chosen as r_o=1200 km. Sensitivity tests show that the dominant radial modes do not differ significantly when the radius of the outer boundary is between 1000 and 1400 km.

3.2.1 Dominant radial modes of the vortex circulation

The symmetric and asymmetric stream functions can be decomposed as

$$\psi_s = \sum_{k=1}^{K} \psi^{(s)}{}_k J_o(\sigma_{ok} r), \qquad (3.13a)$$

$$\psi_a = \sum_{k=1}^{K} J_1(\sigma_{1k}r)\,[\psi^{(a)}_{kc}\cos\lambda + \psi^{(a)}_{ks}\sin\lambda]. \tag{3.13b}$$

Here only the azimuthal wavenumber-one harmonic (beta-gyres) is considered. In Eq. (3.13) r is a non-dimensional radial distance normalized by 1200 km; J_o and J_1 are the zeroth and the first order Bessel function, respectively; σ_{ok} and σ_{1k} are the kth zeroes for J_o and J_1, respectively; $\psi^{(s)}_k$, $\psi^{(a)}_{kc}$ and $\psi^{(a)}_{ks}$ are the coefficients, which are determined by

$$\psi^{(s)}_k = \frac{1}{\pi[J_1(\sigma_{ok})]^2}\int_0^1\int_0^{2\pi}\psi_s J_o(\sigma_{ok}r)\,r\,dr\,d\lambda, \tag{3.14a}$$

$$\psi^{(a)}_{kc} = \frac{2}{\pi[J_2(\sigma_{1k})]^2}\int_0^1\int_0^{2\pi}\psi_a J_1(\sigma_{1k}r)\cos\lambda\,r\,dr\,d\lambda, \tag{3.14b}$$

$$\psi^{(a)}_{ks} = \frac{2}{\pi[J_2(\sigma_{1k})]^2}\int_0^1\int_0^{2\pi}\psi_a J_1(\sigma_{1k}r)\sin\lambda\,r\,dr\,d\lambda. \tag{3.14c}$$

In general, the sum of the first three radial modes matches very well the total symmetric stream function for both case S and W (Figs. 8a,b). The symmetric stream function ψ_s has the largest projection in the second radial mode for case S and in the third radial mode for case W, respectively (figure not shown). The sum of the second and third radial modes approximately describe the total symmetric stream function (Figs. 8a,b).

For the asymmetric streamfunction ψ_a, the first radial mode, $J_1(\sigma_{11}r)$, catches its major feature in case S while the second radial mode, $J_1(\sigma_{12}r)$, has a major contribution in case W (figure not shown). This indicates that the dominant asymmetric radial mode is sensitive to initial symmetric circulation. In case S, the sum of the first three radial modes matches well the total asymmetric streamfunction between the gyre centers, but outside the radius of gyre centers the former has a stronger gradient than the latter because the Bessel function forces streamfunction to be zero at outer radial boundary. In case W, however, the sum of the first three radial modes provides a major portion of the total asymmetric stream function (Fig. 9). Both symmetric and asymmetric circulations can be approximately described in terms of highly-truncated spectral models.

3.2.2 Dominant radial modes in rotational kinetic energy

In terms of radial modes, the symmetric rotational kinetic energy $k_{\psi s}$ can be expressed as, from (3.5a) and (3.13a),

$$K_{\psi s} = \frac{\Delta p \pi}{g} \sum_{k=1}^{K} \sum_{l=1}^{L} \psi^{(s)}{}_k \psi^{(s)}{}_l \alpha_{kl}, \tag{3.15}$$

where

$$\alpha_{kl} = \sigma_{ok}\sigma_{ol} \int_0^1 J_1(\sigma_{ok}r) J_1(\sigma_{ol}r) r dr. \tag{3.15a}$$

Since α_{kl} ($k \neq l$) is very small compared to α_{kl} ($k=l$), $K_{\psi s}$ is calculated only for $k=l$.

Table 3 displays the contribution of each radial mode to $K_{\psi s}$ for both cases. In case S, the second radial mode has a dominant contribution. In case W, however, the third mode contributes the largest portion to $K_{\psi s}$. In each case, the first mode and modes higher than the fourth contribute negligible portion. To the first approximation, the sum of the contributions from the second and third modes accounts for 89% and 90% of the total $K_{\psi s}$ for case S and case W, respectively.

The asymmetric rotational kinetic energy $K_{\psi a}$ is given by, from (3.5b) and (3.13b) (see Appendix),

$$K_{\psi a} = \frac{\Delta p \pi}{2g} \sum_{m=1}^{M} \sum_{l=1}^{L} (\psi^{(a)}{}_{mc}\psi^{(a)}{}_{lc} + \psi^{(a)}{}_{ms}\psi^{(a)}{}_{ls})\,\eta_{ml}, \qquad (3.16)$$

where

$$\eta_{ml} = \frac{1}{2}\sigma_{lm}\sigma_{ll}\int_0^1 [J_o(\sigma_{lm}r)J_o(\sigma_{ll}r)+J_2(\sigma_{lm}r)J_2(\sigma_{ll}r)]rdr. \qquad (3.16a)$$

Again, due to small η_{ml} ($m \neq l$) compared to η_{ml} ($m=l$), $K_{\psi a}$ is computed only for $m=l$.

In case S, the first mode is the largest contributor to $K_{\psi a}$. All modes higher than the second are not important. In case W, the most important contributor is the second mode. The third and the first mode also have significant contributions to $K_{\psi a}$ (Table 4).

In short, as in the circulations, the symmetric (beta-gyre) kinetic energy is dominated by the second (first) radial mode in case S whereas the third (second) radial mode in case W.

3.2.3 Dominant radial normal modes in generation of asymmetric kinetic energy

As mentioned previously, the generation of asymmetric kinetic energy is mainly contributed by the beta-conversion (Eq. (3.9c)). The expansion of the beta-conversion in terms of a Bessel-Fourier series yields

$$CT_3 = \frac{\Delta p \beta \pi r_o}{g} \sum_{k=1}^{K} \sum_{m=1}^{M} \psi^{(a)}_{ms} \psi^{(s)}_{k} \epsilon_{mk}, \tag{3.17}$$

where

$$\epsilon_{mk} = \sigma_{ok} \int_0^1 J_1(\sigma_{1m} r) J_1(\sigma_{ok} r) r dr. \tag{3.17a}$$

and subscripts k and m denote symmetric and asymmetric components, respectively.

In case S, the major contributions to CT_3 come from the interactions between symmetric modes (k=1,2,3) and asymmetric modes (m=1,2), in which the interaction between the second symmetric mode and the first asymmetric mode contributes the largest portion to CT_3 (Table 5a). In case W, contributions to CT_3 are mainly from the interactions between symmetric modes

(k=2,3) and asymmetric modes (m=1,2,3), in particular, the (k=2,m=1), (k=2,m=2), and (k=3,m=2) (Table 5b). In short, the beta-conversions are associated with the first asymmetric radial mode in case S and the second asymmetric radial mode in case W.

3.3 Evolution of beta-gyres associated with the beta-drift

The shallow-water model (2.3) is used in this section to investigate the evolution of the beta-gyres associated with the beta-drift. A horizontal domain 6000×6000 km^2 is chosen with a square mesh of 40 km. Also a sponge layer is used as lateral boundary condition. Cases S and W are integrated for 180 hours.

Figure 10 shows that the vortex in case W follows a looping track, whereas the vortex in case S takes a snake-shaped track. Within the first 48-hour of integration, the tracks in the shallow-water model are similar to those simulated in the dry version of FSU regional model. The natural questions are how the beta-gyres differ in the two cases and how they evolve.

The evolution of the beta-gyres in case W during a major looping period from hour 120 to 162 is illustrated in Figure 11 in terms of the azimuthal wavenumber-one asymmetric stream function. During this period, a pair of stationary outer beta-

gyres are located at 600 km radius with an anticyclonic gyre to the southeast and a cyclonic gyre to the northwest. In contrast, the circulation within 300 km radius (or the inner region) experiences significant changes. Around hour 132, a pair of inner beta-gyres can be identified with an anticyclonic gyre to the north and a cyclonic gyre to the south. The inner beta-gyres rotate counterclockwise and weakens rapidly from hour 132 to hour 144, and the outer beta-gyres dominate afterwards. Note that at hour 126, the west-northwestward drift of the vortex coincides well with the west-northwestward ventilation flow near the vortex center and at hour 162 the northeastward movement also coincides well with the northeastward ventilation flow near the vortex center (Fig. 11). The looping track from hour 120 to 162 appears to be closely associated with variations of the inner and outer beta-gyres.

To see how the outer and inner beta-gyres evolve, the total beta-gyre circulation is partitioned into two components: the first radial mode which represents the outer beta-gyres (Fig. 12) and the residual which denotes the inner beta-gyres (Fig. 13). From hour 120 to hour 162, while its intensity increases with time, the outer beta-gyres are stationary with an anticyclonic gyre to the southeast and a cyclonic gyre to the northwest so that the corresponding ventilation flow is northeastward (Fig. 12). In contrast, from hour 120 to hour 138, the inner beta-gyres develop rapidly and

rotate counterclockwise. From hour 144 to hour 162 the inner beta-gyres decay rapidly as their axis further rotates from due north counterclockwise (Fig. 13).

In summary, the outer beta-gyres are dominated by the first radial mode whereas the inner beta-gyres are well represented by the residual. During a major looping period, the ventilation flow associated with the stationary outer beta-gyres is northeastward. The inner beta-gyres develop rapidly to induce the dominant westward ventilation flow. Then the counterclockwise rotation and decay of the inner beta-gyres result in a change of the ventilation flow direction from the west to northeast. Finally the stationary outer beta-gyres restore the northeastward ventilation flow turning the vortex to the northeast.

Unlike case W, the snake-shaped track in Case S is associated with the evolution of a pair of the beta-gyres (Fig. 14). Initially, the orientation of the gyre axis (as indicated by the azimuthal angle of the anticyclonic-gyre center) is southwest to northeast so that the ventilation flow is toward northwest, which coincides with the northwestward drift. The subsequent clockwise rotation of the beta-gyres turns the ventilation flow to the northeast so that the vortex recurves from the northwest to the northeast. As they continue to rotate clockwise, the beta-gyres weaken and move away from the vortex center. Around hour 156, a new pair of the beta-gyres develop and reestablish the northwestward ventilation

flow around the vortex center causing the recurvature from the northeast to northwest.

It is clear that the difference in the beta-drift between case S and case W stems from the different behavior of the beta-gyres: the clockwise rotation and decay of the original beta-gyres and the development of the new beta-gyres in case S causes a snake-shaped track, whereas the rapid development, counterclockwise rotation and rapid decay of the inner beta-gyres in case W causes a looping track.

The evolution of beta-gyres determines the beta-drift. What causes the counterclockwise rotation of the inner beta-gyres in case W and the clockwise rotation and outward movement of the beta-gyres in case S? The physical processes controlling the azimuthal and radial movement of the beta-gyres will be examined in the next section.

3.4 Azimuthal and radial movement of the beta-gyres

To elucidate the dynamic processes controlling the azimuthal and radial movement of the beta-gyres, a stream function tendency equation in cylindrical coordinates is introduced, the origin of the coordinates being collocated with the center of a drifting vortex (Carr 1987),

$$\frac{\partial\psi}{\partial t} = \nabla^{-2}\{-(\mathbf{V}_s-\mathbf{C})\cdot\nabla\zeta_a \ -(\mathbf{V}_a-\mathbf{C})\cdot\nabla\zeta_s$$

$$-\mathbf{V}_a\cdot\nabla(\zeta_a+f) \ -\mathbf{V}_s\cdot\nabla f\}, \qquad (3.18)$$

where **C** here is a beta-drift velocity, which is independent of radial distance. ∇^{-2} is an inverse Laplacian operator.

To examine the movement of the beta-gyres total streamfunction was partitioned into a symmetric component, a wavenumber-one azimuthal harmonic (beta-gyres) and a residual. Projecting all terms in (3.18) onto wavenumber-one azimuthal harmonic yields the following tendency equation for the beta-gyre streamfunction:

$$\underset{(TT)}{\frac{\partial\psi_{a1}}{\partial t}} = \nabla^{-2}\{\underset{(ASVA)}{-(\mathbf{V}_{a1}-\mathbf{C})\cdot\nabla\zeta_s} \ \underset{(AAVS)}{-\mathbf{V}_s\cdot\nabla\zeta_{a1}} \ \underset{(BETA)}{-\mathbf{V}_s\cdot\nabla f}$$

$$\underset{(ARES)}{-\Lambda_{a1}[(\mathbf{V}_{a1}-\mathbf{C})\cdot\nabla\zeta_{ares}+\mathbf{V}_{ares}\cdot\nabla(\zeta_{a1}+\zeta_{ares}+f)]}\}, \qquad (3.19)$$

where subscripts "a1" and "ares" are, respectively, the beta-gyres and the residual of asymmetric circulation. Symbol Λ_{a1} is an operator for obtaining an azimuthal wavenumber-one component. Term TT is thus the streamfunction tendency for the beta-gyres. Term ASVA is the advection of symmetric vorticity by the asymmetric beta-gyres relative to the drifting velocity of the vortex , term AAVS is the advection of asymmetric vorticity of the beta-gyres by the symmetric flow, term BETA

is the advection of planetary vorticity by the symmetric flow, and term ARES results from the advection of residual vorticity by the beta-gyres relative to the drifting velocity and the advection of absolute vorticity of asymmetric circulation by the residual flow.

In case W the centers of the inner beta-gyres are identified from hour 132 to 143 around 300 km radius, the phase and amplitude evolution of the inner beta-gyres, as well as terms TT, AAVS, ASVS, BETA and ARES at 300 km radius are displayed for that period (Fig. 15). The phase of the inner beta-gyres increases with time, implying that the inner beta-gyres rotate counterclockwise. The rotation rate is about 10° per hour. The phase of the TT is greater than that of the inner beta-gyres so that the TT predicts the counterclockwise rotation of the inner beta-gyres. Further, the term BETA is constant and the term AAVS is much larger than the remaining terms. Since the TT is dominated by the AAVS in amplitude, Eq. (3.19) may be simplified as

$$\frac{\partial \zeta_{al}}{\partial t} = -\mathbf{V}_s \cdot \nabla \zeta_{al}, \tag{3.20}$$

which has a general solution

$$\zeta_{al} = C_k(r)\exp\{i[\lambda-(v_{\lambda s}/r)t]\}, \tag{3.21}$$

where C_k is the amplitude of ζ_{a1} and $v_{\lambda s}$ is the azimuthal wind of the symmetric vortex circulation. Eq. (3.21) shows that the inner beta-gyres rotate counterclockwise, and its rotation rate is determined by $v_{\lambda s}/r$. From hour 132 to hour 143, $v_{\lambda s}$ at 300 km radius is about 15 ms^{-1}. The predicted rotation rate is about 10° per hour, which is very close to that of the numerical simulation.

The phase of the outer beta-gyres at 600 km radius in case W, however, keeps constant from hour 132-143 (Fig. 16), and the phases of the TT and the outer beta-gyres are about the same, implying that the outer beta-gyres are stationary. The TT amplitude is small because the two largest terms, the ASVA and the AAVS are 180° out of the phase and their strengths are about the same so that they cancel each other.

To better understand the clockwise rotation of the beta-gyres in case S, we plotted the phase and amplitude evolution of the beta-gyres, as well as the terms TT, BETA and the sum of AAVS, ASVA and ARES at 750 km radius (Fig. 17) where the centers of the beta-gyres are located. The total tendency TT is almost in phase with the beta-gyres in the first 24 hours so that the beta-gyres were stationary within that period. After 24 hours, the phase of the TT starts to lead clockwise that of the beta-gyres, but the TT amplitude decreases significantly, thus the phase change of the beta-gyres is not significant before hour 60. From hour 60 on the TT amplitude increases with time, and at the same time the TT phase leads

that of the beta-gyres clockwise by 90°. As a result, the beta-gyres rotate clockwise after hour 60. The BETA is controlled by the symmetric vortex. It decreases as the symmetric circulation weakens but remains a constant phase. The sum of the other terms is mainly due to the mutual advection between the symmetric and asymmetric circulations. It increases as the asymmetric circulation develops regardless of the weakening of the symmetric circulation, suggesting that the sum is determined by the asymmetric circulation. In case S, the strong outer flow induces the large rate of the kinetic energy conversion from the symmetric to asymmetric circulation. The rapid decay of the symmetric circulation causes the large amplitude decrease of the BETA. The rapid development of the asymmetric circulation results in the large amplitude increase of the sum. This creates the large amplitude increase of the TT.

To interpret the outward movement of the beta-gyres in case S, radial distributions of the amplitudes of the beta-gyres and the terms TT, ASVA, ARES and the sum of AAVS and BETA are plotted (Fig. 18). The radius of maximum amplitude of beta-gyres is always less than that of TT for both hour 36 and 84, indicating the tendency of outward movement of the beta-gyre centers. At hour 36, the AAVS and the BETA have maximum amplitudes around 350 km radius and are almost out of phase (figure not shown). As a result, their sum is small and almost constant outside 400 km radius. The ASVA contributes the most

to the TT maximum and controls the outward movement. At hour 84, outside 800 km radius the AAVS and the BETA are in phase (figure not shown) so that the sum has a compatible amplitude as the ASVA. Three terms are equally important for the outward movement of the beta-gyres.

3.7 Summary

An extended-range time integration reveals that vortices with different initial symmetric structures may take quite different tracks. The beta-drift is well linked to the evolution of the beta-gyres, which are characterized by development/decay, azimuthal rotation and outward movement. To understand the beta-drift, the dynamics of the beta-gyres is investigated.

The kinetic energy of beta-gyres primarily is converted from symmetric vortex circulation. The rate of kinetic energy conversion from the symmetric to asymmetric circulation is largely determined by the beta-conversion process. The analysis of the beta-conversion reveals that (1) the necessary condition for beta-gyres to intensify is that the anticyclonic gyre must be located to the east of the cyclonic vortex center in the Northern Hemisphere; (2) the rate of the beta-conversion depends on the covariance between the amplitude of the beta-gyres and the RAM of the symmetric vortex. Since the

RAM also controls the amplitude of the beta-gyres, the symmetric vortex structure determines the rate of the beta-conversion. As MRAM increases, the generation rate of asymmetric kinetic energy increases resulting in stronger beta-gyres and a larger beta-drift.

The radial mode analysis shows that the second symmetric radial mode in case S and the third symmetric radial mode in case W dominate symmetric circulation and associated kinetic energy. Corresponding to different symmetric circulations, the first asymmetric radial mode in case S and the second asymmetric radial mode in case W control asymmetric circulation, associated kinetic energy and the beta-conversion.

The azimuthal and radial movement of beta-gyres can be explained by vorticity dynamics. The total tendency is determined by the advection of symmetric vorticity by the asymmetric beta-gyres relative to the beta-drift velocity (ASVA), the advection of asymmetric vorticity of the beta-gyres by the symmetric flow (AAVS), the advection of Earth's vorticity by the symmetric flow (BETA), and the terms arising from the advection of residual vorticity by the beta-gyres relative to the beta-drift velocity and the advection of absolute vorticity of asymmetric circulation by the residual flow (ARES). In case W, the advection of beta-gyre vorticity by the symmetric flow is responsible for the counterclockwise rotation of the inner beta-gyres. In case S, the strong outer

flow causes the large amplitude decrease of the BETA and the large amplitude increase of the sum of AAVS, ASVA and ARES. The large amplitude increase of the total tendency results in the significant clockwise rotation of the beta-gyres. The outward shift of the beta-gyres is controlled by the advection of symmetric vorticity by the beta-gyres relative to the drifting velocity of the vortex.

CHAPTER FOUR

THE EFFECT OF MERIDIONALLY-VARYING ENVIRONMENTAL FLOWS ON PROPAGATION OF A BAROTROPIC VORTEX

The effect of meridionally-varying environmental flows on vortex propagation is investigated with a shallow-water model in this chapter. It focuses on the dynamic processes controlling the intensity variation of asymmetric gyres associated with propagation speed. To carry out energetics analysis, the kinetic energy equations in the presence of environmental flow are derived in section 4.1. Section 4.2 will investigate the dynamic processes responsible for the difference in the propagation speed and associated gyre intensity between constant anticyclonic- and cyclonic-shear cases. Section 4.3 investigates two parabolic-jet cases on a beta-plane in which the environmental absolute vorticity gradients are 2β and 0, respectively, and explains the different evolution of propagation speed and gyre strength. Section 4.4 examines the contributions of a constant-shear and a parabolic-jet to propagation in DeMaria's (1985) wind profile. The last section gives a summary.

4.1 Kinetic energy equations

The shallow-water model B described in chapter two is

used in this chapter. The integration domain of 6000×6000 km^2 is chosen with the square mesh of 40 km. The initial vortex center for all cases is set at 20°N, and located where environmental flows are zero.

The movement of a vortex embedded in a spatially-varying environmental flow is induced by an advection by an environmental steering and a propagation velocity associated with an asymmetric flow of the gyres near the vortex center. To examine the propagation due to the gyres, the track due to the environmental steering at the vortex center is removed from the total vortex track. The residual track is referred to as propagation track.

The propagation of a vortex, which is embedded in a constant-shear or a parabolic-jet flow, is determined by counter-rotating gyres (Williams and Chan 1992). To obtain the gyres associated with propagation, a three-part partition method proposed by Elsberry (1986), and Holland and Evans (1992) was adopted. An asymmetric circulation is obtained by removing a time-independent environmental flow and a symmetric circulation. Further, the asymmetric circulation is partitioned into the first azimuthal mode (the asymmetric gyres) and the residual in terms of a Fourier decomposition in azimuthal direction.

To elucidate the cause of the development of gyres, a set of kinetic energy equations is derived. In the present study the divergent wind is negligible compared to rotational wind.

Thus the rotational wind approximately represents total wind. The vortex circulation consists of the symmetric vortex ($\mathbf{V}_s$), the gyres ($\mathbf{V}_{al}$) and residual ($\mathbf{V}_{arcs}$) of asymmetric circulation, namely,

$$\mathbf{V}_v = \mathbf{V}_s + \mathbf{V}_{al} + \mathbf{V}_{arcs}. \tag{4.1}$$

The horizontal momentum equation for vortex circulation is obtained by subtracting (2.5b) from (2.5a),

$$\frac{\partial \mathbf{V}_v}{\partial t} + \mathbf{V}\cdot\nabla\mathbf{V}_v + f\mathbf{k}\times\mathbf{V}_v = -\nabla\phi_v - \mathbf{V}_v\cdot\nabla\mathbf{V}_c + \mathbf{F}, \tag{4.2}$$

where a friction $\mathbf{F}$ was added.

An area integration is defined as

$$<(\quad)> = \int_o^{ro} r dr \int_o^{2\pi} (\quad) d\lambda. \tag{4.3}$$

Here r_o is a radius of the integrated domain, and r_o=1600 km.

A set of kinetic energy equations is derived by multiplying the horizontal momentum equation (4.2) by $\mathbf{V}_s$, $\mathbf{V}_{al}$, and $\mathbf{V}_{arcs}$, respectively, and integrating these equations by (4.3):

$$\frac{\partial K_s}{\partial t} = F_s - (K_s,\ K_{al}) - (K_s,\ K_{arcs}) + (K_c,\ K_s) + D_s, \tag{4.4a}$$

$$\frac{\partial K_{al}}{\partial t} = F_{al}+(K_s,\ K_{al})+(K_{arcs},\ K_{al})+(K_c,\ K_{al})+D_{al}, \qquad (4.4b)$$

$$\frac{\partial K_{arcs}}{\partial t} = F_{arcs}+(K_s,\ K_{arcs})-(K_{arcs},\ K_{al})+(K_c,\ K_{arcs})+D_{arcs}, \qquad (4.4c)$$

where F_s, F_{al}, and F_{arcs} are the energy fluxes due to radial flows evaluated at the outer radial boundary of the integration domain, D_s, D_{al}, and D_{arcs} are the dissipation terms.

The energy conversion terms in Eq. (4.4) are defined as follows:

$$(K_s,\ K_{al}) = -\langle(\mathbf{V}\cdot\nabla\mathbf{V}_s)\cdot\mathbf{V}_{al}\rangle + \langle f\mathbf{k}\cdot(\mathbf{V}_{al}\times\mathbf{V}_s)\rangle, \qquad (4.5a)$$

$$(K_s,\ K_{arcs}) = -\langle(\mathbf{V}\cdot\nabla\mathbf{V}_s)\cdot\mathbf{V}_{arcs}\rangle + \langle f\mathbf{k}\cdot(\mathbf{V}_{arcs}\times\mathbf{V}_s)\rangle, \qquad (4.5b)$$

$$(K_{arcs},\ K_{al}) = -\langle(\mathbf{V}\cdot\nabla\mathbf{V}_{arcs})\cdot\mathbf{V}_{al}\rangle + \langle f\mathbf{k}\cdot(\mathbf{V}_{al}\times\mathbf{V}_{arcs})\rangle, \qquad (4.5c)$$

$$(K_c,\ K_{\psi s}) = -\langle(\mathbf{V}_v\cdot\nabla\mathbf{V}_c)\cdot\mathbf{V}_s\rangle, \qquad (4.5d)$$

$$(K_c,\ K_{al}) = -\langle(\mathbf{V}_v\cdot\nabla\mathbf{V}_c)\cdot\mathbf{V}_{al}\rangle, \qquad (4.5e)$$

$$(K_c,\ K_{arcs}) = -\langle(\mathbf{V}_v\cdot\nabla\mathbf{V}_c)\cdot\mathbf{V}_{arcs}\rangle, \qquad (4.5f)$$

where $\mathbf{V}_v = \mathbf{V} - \mathbf{V}_c$.

4.2 Intensity of gyres and vortex propagation in constant-shear cases

In this section, three experiments were conducted. Case C_0 has a resting environment. Cases C_1 and C_2 have a constant-

shear zonal environmental flow, which is expressed as

$$u_c = u_{cy}(y-y_o), \tag{4.6}$$

where u_c is a meridionally-varying zonal flow, y_o is the latitude of initial vortex center. Cases C_1 and C_2 have u_{cy} of $5.875\times10^{-6}\,s^{-1}$ and $-5.875\times10^{-6}\,s^{-1}$, respectively. Therefore, case C_1 has an anticyclonic-shear whereas case C_2 has a cyclonic-shear environmental flow. An azimuthal wind profile of an initial vortex for all three cases was chosen with V_m=30 ms^{-1}, r_m=100 km, R_o=750 km in Eq. (3.2a).

The propagation tracks of the vortices (Fig. 19) for both constant-shear cases are similar to those of Williams and Chan (1992). The constant anticyclonic-shear case (case C_1) has the longest propagation track whereas the constant cyclonic-shear case (case C_2) has the shortest propagation track among three cases. For example, the propagation speeds in cases C_1, C_o, and C_2 at hour 48 are 3.49, 2.34, 2.05 ms^{-1}, respectively.

The propagation speed of the vortex is determined by the strength of the gyres (Fig. 20), which can be well measured by the amount of kinetic energy. To interpret the difference in propagation speeds among three cases, the kinetic energy budgets were computed at hour 48 (Fig. 21). The larger and smaller propagation speeds in case C_1 and C_2 are consistent with the larger and smaller K_{a1} (or the stronger and weaker gyres), respectively, compared to those in case C_o. There are

three possible energy conversions associated with the change of K_{al} in the constant-shear cases. The most important process is the conversion between K_c and K_{al}, although this conversion rate is smaller than the rate of conversion from K_s to K_{al}. Case C_1 favors the conversion from K_c to K_{al} whereas case C_2 allows the conversion from K_{al} to K_c. The rate of conversion from K_s to K_{al} is larger in case C_1 whereas smaller in case C_2 than that in case C_o, which also contribute to the differences of K_{al}. The conversion between K_{al} and K_{arcs}, however, is negligible compared to the other conversions. In case C_1 the energy is converted from K_s, K_c to K_{al} so that the gyres develop at a higher rate. In case C_2, however, the energy converting from K_s to K_{al} overcomes the loss of K_{al} due to the conversion from K_{al} to K_c so that the gyres grow at a lower rate.

The propagation tracks from Fig. 19 also reveal that the displacement difference between cases C_1 and C_o is much longer than that between cases C_2 and C_o. From Fig. 21, it is seen that the rate of conversion from K_c to K_{al} in case C_1 is twice as large as that in case C_2. Also the rate difference of conversion from K_s to K_{al} between cases C_1 and C_o is three times as large as that between cases C_2 and C_o. Therefore, the difference of K_{al} between cases C_1 and C_o is much larger than that between cases C_2 and C_o.

Since the conversion between K_c and K_{al} is an important physical process determining the magnitude difference of K_{al} between case C_1 and case C_2, it deserves further analysis. In

cylindrical coordinates, it can be expressed as

$$(K_c,\ K_{al}) = -\langle v_{ral}^2 \frac{\partial v_{rc}}{\partial r} + \frac{v_{\lambda al}^2}{r}\left(\frac{\partial v_{\lambda c}}{\partial \lambda} + v_{rc}\right)$$

$$+ v_{ral} v_{\lambda al}\left[\frac{\partial v_{rc}}{r\partial \lambda} + r\frac{\partial}{\partial r}\left(\frac{v_{\lambda c}}{r}\right)\right]\rangle, \qquad (4.7)$$

where v_{ral} and $v_{\lambda al}$, v_{rc} and $v_{\lambda c}$ are the radial and azimuthal wind components of the gyres, and the constant-shear flow, respectively.

For simplicity, the streamfunction of the gyres can be expressed as

$$\psi_{al} = R_a(r)\cos(\alpha-\lambda), \qquad (4.8)$$

where R_a is the amplitude of the gyres and α is an azimuthal angle of the anticyclonic-gyre center, measured counterclockwise from due north. Here α is independent of the radial distance so that the effect of the radial phase tilt of the gyres is not considered.

The constant-shear flow (4.6) has the following form in cylindrical coordinates,

$$v_{rc} = -0.5ru_{cy}\sin 2\lambda, \qquad (4.9a)$$

$$v_{\lambda c} = -0.5ru_{cy}(1+\cos 2\lambda). \qquad (4.9b)$$

Substituting (4.8) and (4.9) into (4.7) yields

$$(K_c, K_{al}) = -0.5u_{cy}\sin 2\alpha K_{al}. \qquad (4.10)$$

Since the axis of the gyre centers orients southwest-northeast in the present cases, or $-\pi/2<\alpha<0$, $-\sin 2\alpha$ is always positive.

From (4.10), therefore, two inferences can be made.

(1) The sign of conversion between K_c and K_{al} is determined by the sign of constant-shear flow. An anticyclonic-shear (with a positive u_{cy}) allows a kinetic energy conversion from K_c to K_{al} so that K_{al} is gained (see case C_1 in Fig. 21) whereas a cyclonic-shear (with a negative u_{cy}) favors a kinetic energy conversion from K_{al} to K_c so that K_{al} is lost (see case C_2 in Fig. 21).

The rate of conversion between K_c and K_{al} is proportional to the magnitude of constant-shear flow. The stronger the constant anticyclonic-(cyclonic-) shear flow is, the longer (shorter) the propagation track is. Within 72-hour integrations, the lengths of the propagation tracks for the constant anticyclonic-shear flows with the magnitudes of $2.94\times10^{-6}s^{-1}$, 5.875×10^{-6} s^{-1} and $1.175\times10^{-5}s^{-1}$ are 497, 592 and 789 km, respectively. The lengths of the propagation tracks for the constant cyclonic-shear flows with the magnitudes of -2.94×10^{-6} s^{-1}, $-5.875\times10^{-6}s^{-1}$ and -1.175×10^{-5} s^{-1} are 421, 394 and 354 km, respectively.

(2) The rate of conversion from K_c to K_{a1} is approximately proportional to K_{a1}. Therefore, in constant anticyclonic-shear case, this conversion term generates more K_{a1}, causing stronger gyres and a larger propagation whereas in constant cyclonic-shear case, the conversion term destroys K_{a1}, resulting in weaker gyres and a smaller propagation.

4.3 Evolution of gyre intensity and vortex propagation in parabolic-jet cases

Two cases were tested in which a parabolic-type zonal environmental flow is included:

$$u_c = \frac{1}{2} u_{cyy} (y-y_o)^2 \qquad (4.11)$$

The values of u_{cyy} in cases D_1 and D_2 are β and $-\beta$ at 20°N, respectively. The environmental absolute vorticity gradient is, therefore, zero in case D_1 and 2β in case D_2. Both cases have an identical azimuthal wind profile for the initial vortex as in case C_o.

Figure 22 shows the propagation tracks for the parabolic-jet cases in comparison with the track for case C_o during 108-hour integrations, which are similar to those displayed by Williams and Chan (1992). The vortex in case D_1 moves much slower in the first 48 hours but much faster in the last 48

hours than that in case D_2. For example, the propagation speeds for cases D_1, C_o and D_2 are 0.72, 1.23, and 2.29 ms^{-1} at hour 24, while they are 2.82, 2.63, and 1.46 ms^{-1} at hour 96, respectively. The evolution of the propagation speed is consistent with the intensity evolution of the gyres (Fig. 23). In this section, a kinetic energy analysis is carried out to explain the different evolution of the vortex propagation in cases D_1 and D_2.

At hour 24, the K_{a1} in case D_1 is smaller whereas that in case D_2 is larger than that in case C_o. The smaller rate of conversion from K_s to K_{a1} generates less K_{a1} in case D_1 whereas the larger rate results in more K_{a1} in case D_2 (Fig. 24). Therefore, case D_1 shows a smaller vortex propagation than case D_2.

Notice that the kinetic energy is converted from K_c to K_s in case D_1 whereas it is converted from K_s to K_c in case D_2. Thus the K_s in case D_1 becomes much larger than that in case D_2 around hour 96 (Fig. 25). Correspondingly, the rate of the conversion from K_s to K_{a1} becomes much larger in case D_1 than that in case D_2. Although the rate of conversion from K_{a1} to K_c and K_{arcs} in case D_1 is larger than that in case D_2, the generation rate of K_{a1} in case D_1 is greater than that in case D_2, resulting in the largest K_{a1} of case D_1 among three cases.

Since the conversion (K_c, K_s) and conversion (K_s, K_{a1}) are important in determining the intensity evolution of the gyres, they are worth to be theoretically analyzed further.

In cylindrical coordinates, (K_c, K_s) can be expressed as

$$(K_c, K_s) = -\langle v_{\lambda a1}\left(\frac{\partial v_{\lambda c}}{\partial r} + \frac{v_{\lambda c}}{r}\right) v_{\lambda s}\rangle, \tag{4.12}$$

and a parabolic-jet flow (4.11) has the following expression

$$v_{rc} = -0.125 u_{cyy} r^2 (\sin\lambda + \sin 3\lambda), \tag{4.13a}$$

$$v_{\lambda c} = -0.125 u_{cyy} r^2 (3\cos\lambda + \cos 3\lambda). \tag{4.13b}$$

Assume that the streamfunction of the gyres has the same form as (4.8). Inserting (4.8) and (4.13) in (4.12) yields

$$(K_c, K_s) = 0.25\pi u_{cyy}[\sin\alpha \int_o^{r_o} R_a r^3 \frac{\partial}{\partial r}\left(\frac{v_{\lambda s}}{r}\right)]. \tag{4.14}$$

The values in the square bracket are positive in both parabolic-jet cases because the anticyclonic gyre is located to the east of the vortex center so that $\sin\alpha<0$ and the azimuthal angular wind $(v_{\lambda s}/r)$ decreases with increasing radial distance for the current vortex profile. Thus the sign of conversion between K_c and K_s is determined by the sign of parabolic-jet flow. The parabolic-jet flow with a positive u_{cyy} in case D_1 favors the conversion from K_c to K_s, whereas that with a negative u_{cyy} in case D_2 causes the conversion from K_s to K_c.

The conversion from K_s to K_{a1} is expressed as

$$(K_s,\ K_{al}) = -\langle(\mathbf{V}_{al}\cdot\nabla\mathbf{V}_s)\cdot\mathbf{V}_{al}\rangle + \langle\beta r\cos\lambda\mathbf{k}\cdot(\mathbf{V}_{al}\times\mathbf{V}_s)\rangle$$
$$-\langle(\mathbf{V}_c\cdot\nabla\mathbf{V}_s)\cdot\mathbf{V}_{al}\rangle, \qquad (4.15)$$

where the first and the second term of rhs are, respectively, the nonlinear-conversion (CT_1) and the beta-conversion (CT_3) (see discussions in chapter three). The third term of rhs is the additional term (CT^*_3) due to the presence of the parabolic-jet flow.

At hour 24, the rates of the beta-conversion for three cases are about the same (Table 6a). A positive CT^*_3 and a negative CT^*_3, respectively, create the larger and smaller rates of conversion from K_s to K_{al} in case D_1 and case D_2 compared to that in case C_o.

At hour 96, much stronger symmetric vortex circulation creates much larger rate of conversion from K_s to K_{al} through the beta-conversion in case D_1 than those in cases D_2 and C_o (Table 6b).

4.4 Analysis of DeMaria's wind profile

The relative vorticity gradient of environmental flow plays a similar role as the planetary vorticity gradient in vorticity balance. It is often considered as an important factor affecting tropical cyclone motion in the previous studies (e.g., Kasahara 1957). DeMaria (1985) considered a

zonal environmental flow, which can be expressed as

$$u_c = u_m\left(\frac{y-y_c}{y_m}\right)\exp\left\{-\frac{1}{2}\left[1-\left(\frac{y-y_c}{y_m}\right)^2\right]\right\}, \qquad (4.16)$$

where y_c is the latitude where u_c changes sign and y_m is the distance from y_c to the latitude of maximum or minimum zonal speed u_m. He chose y_c=2000 km, y_m=600 km, u_m=-10 ms^{-1} for positions A-C, and u_m=10 ms^{-1} for positions D-F (Fig. 26a). The vorticity of the flow holds the large negative values at positions A-C whereas the large positive values at positions D-F (Fig. 26b). From position C (F) to position A (D), the relative vorticity gradient of the flow changes from negative to positive values (Fig. 26c).

Using an identical initial vortex as that in case C_o, 72-hour integrations (Fig. 27) display that the vortex tracks for initial positions A-C diverge whereas the tracks for initial positions D-F converge, which are similar to those showed by DeMaria (1985). DeMaria interpreted that since the absolute vorticity gradient at positions A-C (D-F) increases (decreases) northward, the northwestward drift of the vortex will be increased (decreased), and the vortex tracks diverge (converge). Because a strong anticyclonic- (cyclonic-) shear appears at positions A-C (D-F), this section examines the contributions of the constant-shear as well as the parabolic-jet to the propagation track.

Figure 28 shows the propagation tracks corresponding to Figure 27. The vortices placed at positions A-C have the northwestward propagation tracks. The northward components of the propagation tracks at positions A-B have the same length as that in the constant anticyclonic-shear case with the magnitude of $10^{-5}\ s^{-1}$ (figure not shown), but the westward components of the formers are longer than that of the latter. This may suggest that the strong anticyclonic-shear controls the northward propagation whereas the parabolic-jet influences the westward propagation for vortices at positions A-B. The vortex initially placed at position C shows small propagation track within the first 24 hours because the absolute vorticity gradient is -0.5β, and later on it has the compatible length of the propagation track as those at positions A and B, indicating the effect of the strong anticyclonic-shear on vortex propagation.

The vortices initially placed at positions D-F have the north-northwest, north-northeast and east-northeast propagation, respectively (Fig. 28). The vortices at positions D-F apparently have shorter propagation tracks than those at positions A-C. The vortex initially placed at position E, where the cyclonic-shear is the strongest, has the smallest propagation, implying that the cyclonic-shear has the influence on the propagation speed. Parabolic-jet cases on a beta-plane in which the environmental absolute vorticity gradients are -0.5β and $-\beta$ show the northeastward and east-

northeastward propagation, respectively (figure not shown). The vortex at position D recurves from the northwest to the north because the absolute vorticity gradient changes from 1.5β to 0. The vortex at position E has the north-northeastward propagation since the absolute vorticity gradient varies from β to -0.5β. The vortex at position F moves east-northeastward because the absolute vorticity gradient varies from -0.5β to $-\beta$ as the vortex moves northward.

Analysis of DeMaria's wind profile suggests that the constant-shear and the parabolic-jet have equally important effect on the vortex propagation.

4.5 Summary

Meridionally-varying environmental flows (constant-shear and parabolic-jet) affect the vortex propagation via changing gyres, whose flow over the vortex center advects symmetric vorticity. An energetics analysis was carried out to investigate the dynamic processes responsible for the intensity variation of gyres associated with vortex propagation speed in the presence of the environmental flows.

The energy conversion between environmental flow and asymmetric gyres is an important process responsible for the intensity difference of gyres between the constant

anticyclonic- and cyclonic-shear cases. The kinetic energy is converted from the environmental flow to gyres in the constant anticyclonic-shear case, whereas it is converted from the gyres to environmental flow in the constant cyclonic-shear case. As a result, the gyres in the constant anticyclonic-shear case are stronger while those in the constant cyclonic-shear case are weaker than the gyres in the case with no environmental flow. This causes a larger vortex propagation in the constant anticyclonic-shear case than that in the constant cyclonic-shear case.

Two tests in the parabolic-jet cases on a beta-plane were carried out in which the absolute vorticity gradients of environmental flows are zero (case D_1) and 2β (case D_2). The vortex in case D_1 follows a slower propagation first and a faster propagation later than that in case D_2. Initially, Case D_2 generates more energy through the conversion from K_s to K_{a1}, causing stronger gyres and a larger propagation than case D_1. For parabolic-jet cases, the kinetic energy exchange between environmental and symmetric flows plays a key role in controlling the intensity evolution of gyres. The kinetic energy is converted from the environmental to symmetric flows persistently so that the symmetric vortex dramatically develops in case D_1 whereas it is converted from the symmetric to environmental flows so that the symmetric vortex weakens in case D_2. Thus the rates of the beta-conversion as well as the asymmetric kinetic energy generation become much larger in

case D_1 than that in case D_2. This results in strong development of the gyres and the acceleration of the vortex propagation in case D_1.

CHAPTER FIVE

CONCLUSIONS

This dissertation research focuses on the dynamics of vortex propagation and associated counter-rotating gyres for a vortex being embedded in a quiescent environment and in meridionally-varying environmental flows. Both a dry version of FSU regional model and a shallow-water model are adopted to examine these issues.

The first important result of this research is to figure out how beta-gyres develop and the necessary and favorable conditions for development of beta-gyres. An energetics diagnosis reveals that beta-gyres develop by extracting kinetic energy from the symmetric circulation of the vortex. This energy conversion is mainly associated with the planetary advection and the horizontal momentum advection. The former (referred to as beta-conversion) contributes the most to the generation of kinetic energy for development of beta-gyres.

Further analysis of the beta-conversion reveals that (1) the beta-gyres can develop only when an anticyclonic gyre is located to the east of the cyclonic vortex center in the Northern Hemisphere, and (2) the rate of the beta-conversion is proportional to the covariance between the amplitude of the beta-gyres and the RAM of the symmetric vortex circulation. A vortex with a strong outer flow or a larger MRAM creates a stronger initial beta-gyres. The stronger gyres interacting

with the stronger outer symmetric flow generate more asymmetric kinetic energy via the larger rate of the beta-conversion, resulting in a faster drift.

The second important result of this research is demonstration that in a quiescent environment on a beta-plane vortices with different initial symmetric structures follow substantially different tracks. The unsteady tracks are associated with the evolution of the beta-gyres, which are characterized by intensity variation, azimuthal rotation and outward movement.

The azimuthal and radial movement of beta-gyres is predicted by streamfunction tendency of beta-gyres. The total tendency is determined by the advection of symmetric vorticity by the asymmetric beta-gyres relative to the vortex drifting velocity (ASVA), the advection of asymmetric vorticity of beta-gyres by the symmetric flow (AAVS), the advection of planetary vorticity by the symmetric flow (BETA), and the terms resulting from the advection of residual vorticity by beta-gyres relative to the vortex drifting velocity and the advection of asymmetric absolute vorticity by the residual flow (ARES). For the inner beta-gyres whose centers are near the radius of maximum cyclonic wind, the advection of beta-gyre vorticity by symmetric flow is a dominant process responsible for their counterclockwise rotation. For the outer beta-gyres whose centers are around the periphery of the cyclonic azimuthal wind, their clockwise rotation is caused by

a decrease in the BETA and an increase in the sum of AAVS, ASVA and ARES, and their outward movement is mainly caused by the advection of symmetric vorticity by the beta-gyres relative to the beta-drift velocity.

The third important result of this research is to explain how meridionally-varying environmental flow (constant-shear and parabolic-jet) affects asymmetric gyres and vortex propagation.

In constant-shear cases, an anticyclonic-shear causes a faster propagation than a cyclonic-shear. The propagation speed is consistent with the intensity of counter-rotating gyres. The kinetic energy exchange between the gyres and environmental flow is a key process responsible for the intensity difference of gyres. The constant anticyclonic-shear favors for kinetic energy conversion from the environmental flow to gyres whereas the constant cyclonic-shear allows kinetic energy conversion from the gyres to environmental flow. Therefore, strong gyres induce a fast vortex propagation in the constant anticyclonic-shear case while weak gyres cause a slow vortex propagation in the constant cyclonic-shear case.

Two experiments of parabolic-jet cases on a beta-plane were carried out in which the environmental absolute vorticity gradient is zero (case D_1) and 2β (case D_2). In the first 48 hours the vortex in case D_1 propagates slower than that in case D_2, but after 48 hours the vortex in case D_1 propagates faster than that in case D_2. The energy conversion from the

symmetric circulation to gyres has a larger rate in case D_2 than that in case D_1 initially so that the gyres are stronger in case D_2 than that in case D_1. As time goes on, the energy is persistently transferred from the environmental to symmetric flow in case D_1 whereas it is converted from the symmetric to environmental flow in case D_2 so that the symmetric circulation becomes much stronger in case D_1 than that in case D_2. The stronger symmetric circulation produces the larger rate of the asymmetric kinetic energy generation in case D_1 than that in case D_2. As a result, the gyres become stronger causing a larger vortex propagation in case D_1 than those in case D_2.

APPENDIX

Derivations of Eqs. (3.16) and (3.16a)

The asymmetric rotational kinetic energy ($K_{\psi a}$) is defined as,

$$K_{\psi a} = < \frac{\nabla\psi_a \cdot \nabla\psi_a}{2} >, \qquad \text{(A1)}$$

where ψ_a is asymmetric component of stream function; and the angle bracket here is,

$$<(\qquad)> = \frac{\Delta p}{g}\int_0^{ro} r dr \int_0^{2\pi} (\qquad) d\lambda, \qquad \text{(A2)}$$

where Δp = 150 mb here.

For convenience, radial distance $r = r_o r'$, in which r_o = 1200 km here, and r' is a dimensionless radial distance.

Applying (A2) on (A1) yields,

$$K_{\psi a} = \frac{\Delta p}{2g}\int_0^1 r_o^2 r dr \int_0^{2\pi} [(\frac{\partial\psi_a}{r_o r \partial\lambda})^2 + (\frac{\partial\psi_a}{r_o \partial r})^2] d\lambda, \qquad \text{(A3)}$$

where prime of r is omitted, and r is a dimensionless radial distance.

Using Eq. (3.13b) leads to

$$\frac{\partial\psi_a}{r\partial\lambda} = \sum_{m=1}^{M} \frac{J_1(\sigma_{1m}r)}{r}[-\psi^{(a)}{}_{mc}\sin\lambda + \psi^{(a)}{}_{ms}\cos\lambda], \tag{A4a}$$

$$\frac{\partial\psi_a}{\partial r} = \sum_{m=1}^{M} \frac{\partial J_1(\sigma_{1m}r)}{\partial r}[\psi^{(a)}{}_{mc}\cos\lambda + \psi^{(a)}{}_{ms}\sin\lambda]. \tag{A4b}$$

Substituting (A4) into (A3) yields

$$K_{\psi a} = \frac{\Delta p\pi}{2g} \sum_{m=1}^{M} \sum_{l=1}^{L} (\psi^{(a)}{}_{mc}\psi^{(a)}{}_{lc} + \psi^{(a)}{}_{ms}\psi^{(a)}{}_{ls}) \cdot$$

$$\int_0^1 [\frac{J_1(\sigma_{1m}r)}{r} \frac{J_1(\sigma_{1l}r)}{r} + \frac{\partial J_1(\sigma_{1m}r)}{\partial r} \frac{\partial J_1(\sigma_{1l}r)}{\partial r}]rdr. \tag{A5}$$

Bessel function has the following relations

$$\frac{\partial J_1(\sigma_{1m}r)}{\partial r} = \frac{\sigma_{1m}}{2} [J_o(\sigma_{1m}r) - J_2(\sigma_{1m}r)],$$

$$\frac{J_1(\sigma_{1m}r)}{r} = \frac{\sigma_{1m}}{2} [J_o(\sigma_{1m}r) + J_2(\sigma_{1m}r)]. \tag{A6}$$

Using (A6) in (A5), finally, yields

$$K_{\psi a} = \frac{\Delta p\pi}{2g} \sum_{m=1}^{M} \sum_{l=1}^{L} (\psi^{(a)}{}_{mc}\psi^{(a)}{}_{lc} + \psi^{(a)}{}_{ms}\psi^{(a)}{}_{ls})\eta_{ml}, \tag{3.16}$$

where

$$\eta_{ml} = \frac{1}{2}\sigma_{1m}\sigma_{1l}\int_0^1 [J_o(\sigma_{1m}r)J_o(\sigma_{1l}r)+J_2(\sigma_{1m}r)J_2(\sigma_{1l}r)]rdr. \tag{3.16a}$$

Table 1 The kinetic energy components $K_{\psi s}$ (10^{17}J), $K_{\psi a}$ (10^{15}), the energy flux $F_{\psi a}$ and the conversion from $K_{\psi s}$ to $K_{\psi a}$ ($10^{11}Js^{-1}$) calculated at hour 6 for case S and case W.

	$K_{\psi s}$	$K_{\psi s}$	$F_{\psi a}$	($K_{\psi s}$, $K_{\psi a}$)
case S	12.3	6.8	-0.25	4.55
case W	4.9	3.1	0.003	0.96

Table 2 The breakdown of conversion from $K_{\psi s}$ to $K_{\psi a}$ at hour 6 for case S and case W (unit: Js^{-1}). See Eq. (3.9) for the definitions of CT_1, CT_2 and CT_3.

	CT_1 (10^{11})	CT_2 (10^{8})	CT_3 (10^{11})
case S	-0.18	-2.60	4.73
case W	0.25	-6.68	0.70

Table 3 Contribution of each symmetric radial mode to $K_{\psi s}$ at hour 24 for case S and case W (unit: 10^{17}J)

k	1	2	3	4	5	6
case S	0.0560	1.2695	0.2375	0.0935	0.0062	0.0269
case W	0.0001	0.1820	0.3907	0.0410	0.0189	0.0056

Table 4 contribution of each asymmetric radial mode to $K_{\psi a}$ at hour 24 for case S (unit: 10^{16} J) and case W (unit: 10^{15} J)

m	1	2	3	4
case S	1.2205	0.3361	0.0598	0.0886
case W	0.2692	0.6414	0.4061	0.1489

Table 5 Components of interaction between symmetric and asymmetric radial modes in the beta-conversion (CT_3) at hour 24 for (a) case S (10^{11} Js^{-1}) and (b) case W (10^{10} Js^{-1})

(a)

k \ m	1	2	3	4
1	0.7835	0.0749	0.0150	0.0109
2	1.8173	-0.7135	-0.0828	-0.0522
3	-0.2061	-0.2254	0.0914	0.0323
4	0.0626	0.0404	0.0462	-0.0541

(b)

k \ m	1	2	3	4
1	0.0477	-0.0098	-0.0024	-0.0011
2	1.0231	0.8663	0.1223	0.0506
3	-0.3931	0.9272	-0.4573	-0.1063
4	0.0616	-0.0858	-0.1192	0.0918

Table 6 Calculations of CT_1, CT_3 and CT^*_3 in cases D_1, C_o and D_2 at (a) hour 24, and (b) hour 96 (unit: 10^7 m^4s^{-1}). See Eq. (4.15) for the definitions of CT_1, CT_3 and CT^*_3.

(a)

case	CT_1	CT_3	CT^*_3
D_1	-0.04	2.53	-0.73
C_o	-0.50	2.55	0.00
D_2	-0.50	2.76	1.13

(b)

case	CT_1	CT_3	CT^*_3
D_1	-1.99	13.24	-6.24
C_o	-0.45	3.16	0.00
D_2	-0.15	2.01	0.92

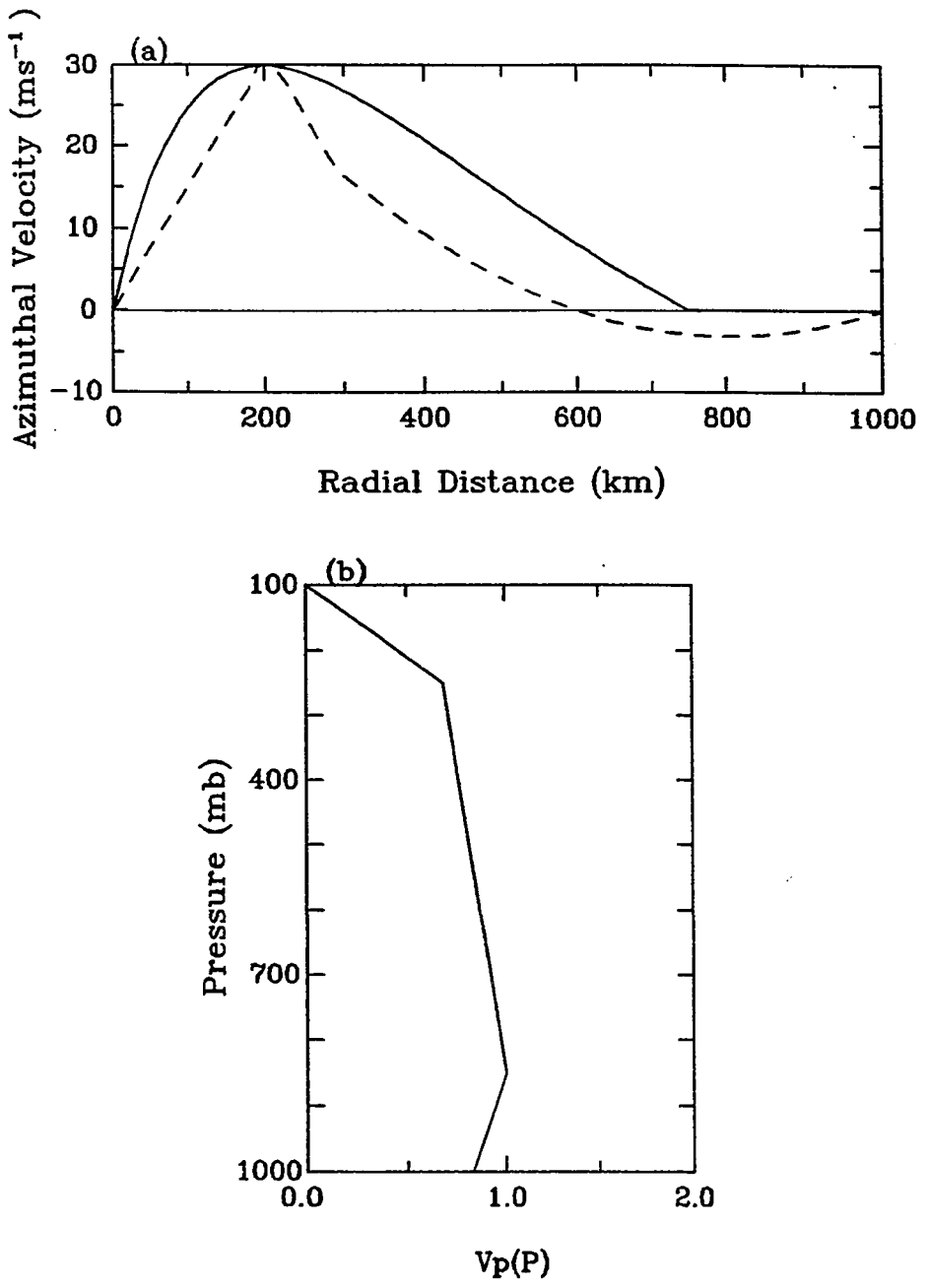

Fig. 1 (a) Azimuthal wind profiles of initial symmetric vortices for case S (solid) and case W (dashed) and (b) vertical wind profile of initial symmetric vortices for case S and case W.

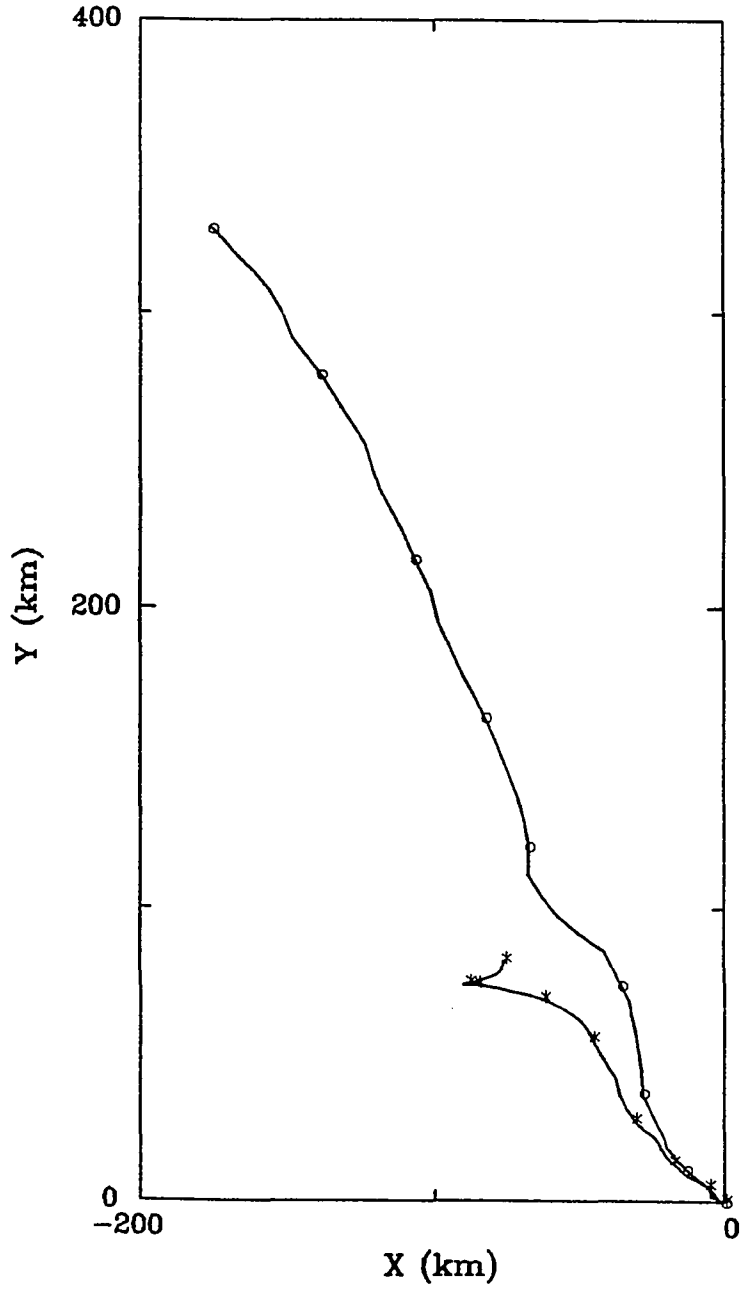

Fig. 2 Vortex tracks at 6-hour interval for case S (O), case W (*) during 48-hour integrations using a dry version of FSU regional model. Abscissa and ordinate units are km.

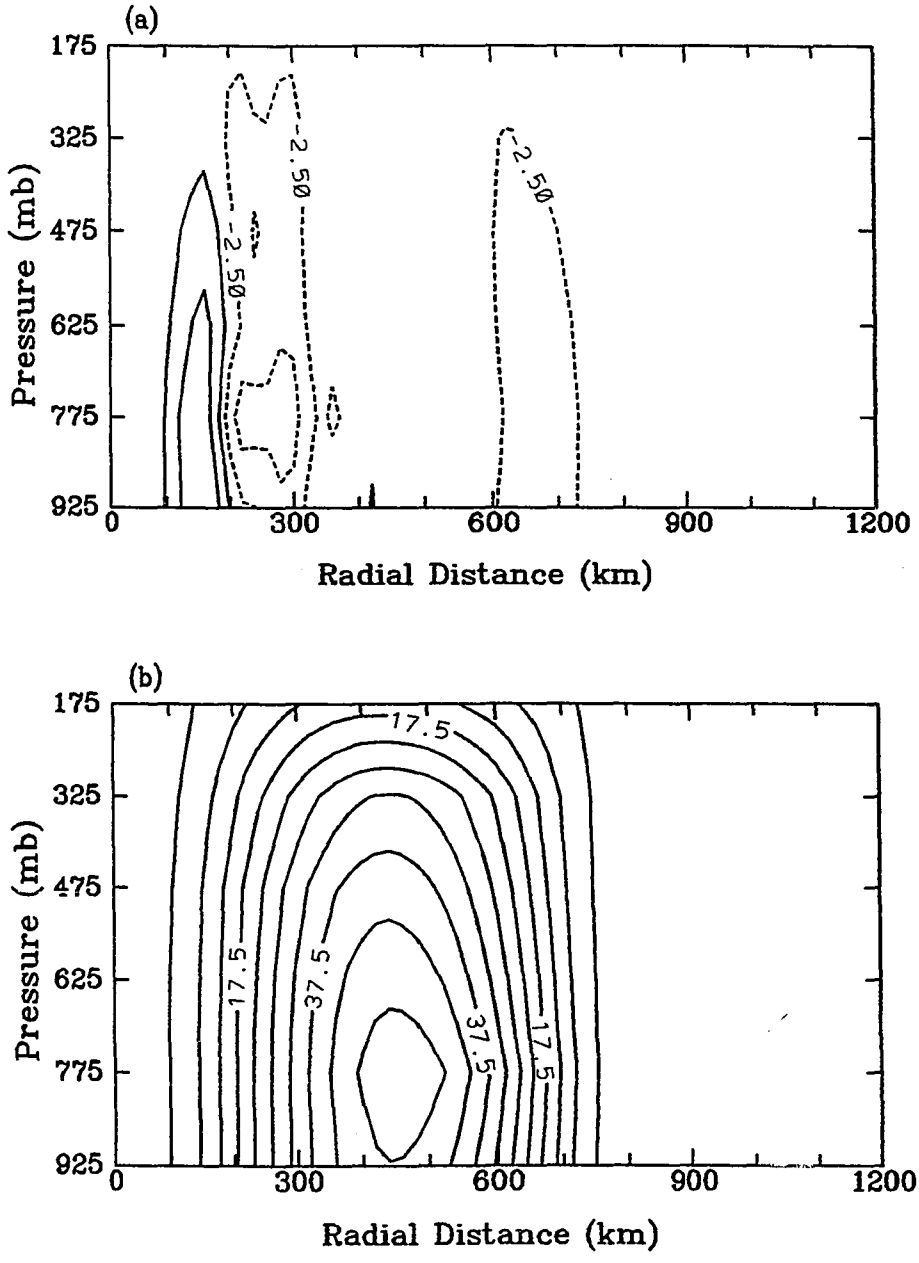

Fig. 3 The vertical-radial distributions of (a) the nonlinear-conversion and (b) the beta-conversion with a contour interval of 5×10^{8} Js^{-1} at hour 6 for case S.

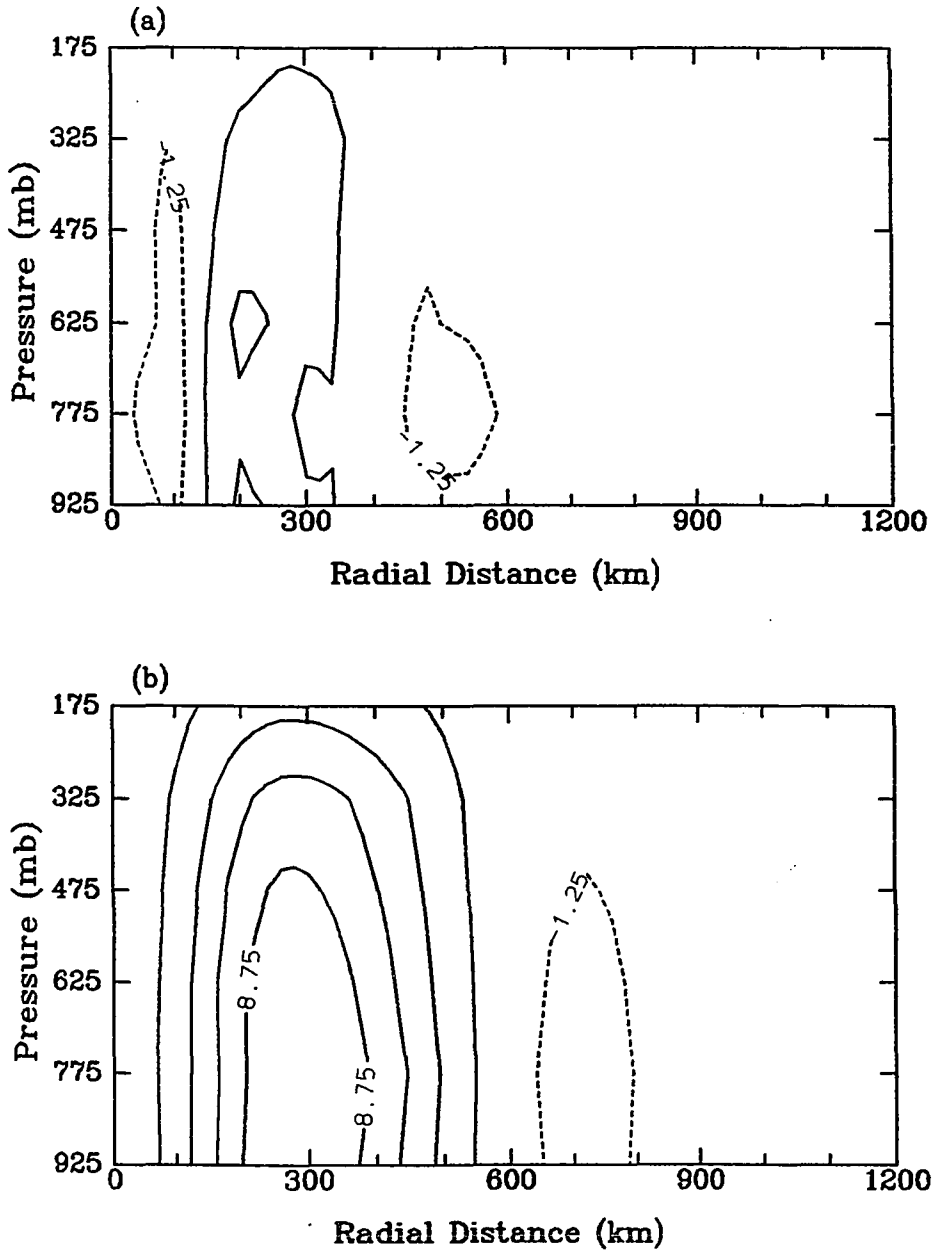

Fig. 4 As in Fig. 3 except for case W with a contour interval of 2.5×10^{8} Js^{-1}.

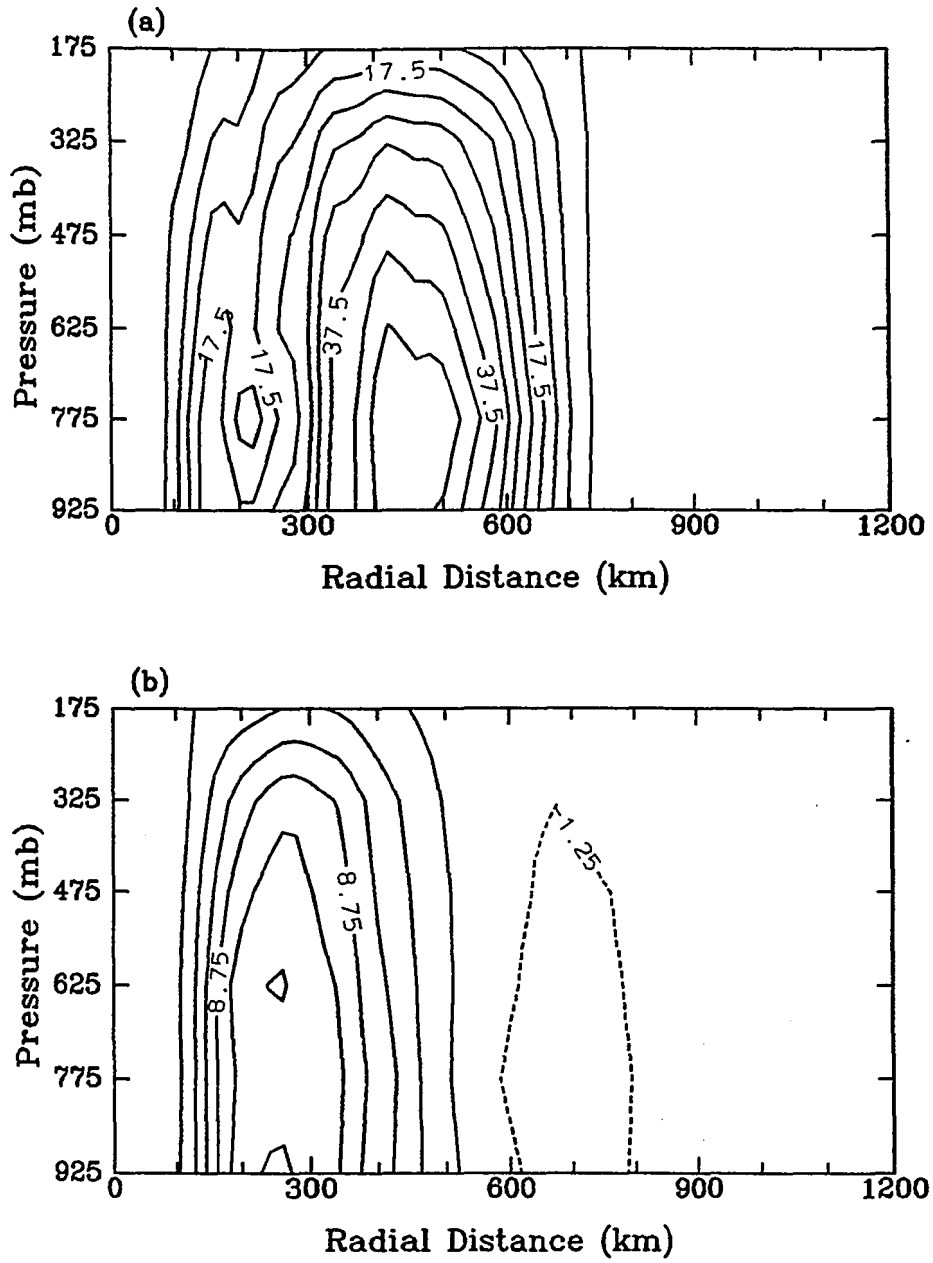

Fig. 5 The vertical-radial distributions of conversion from K_{ψ_a} to K_{ψ_a} at hour 6 for (a) case S (contour interval of 5×10^8 Js^{-1}) and (b) case W (contour interval of 2.5×10^8 Js^{-1}).

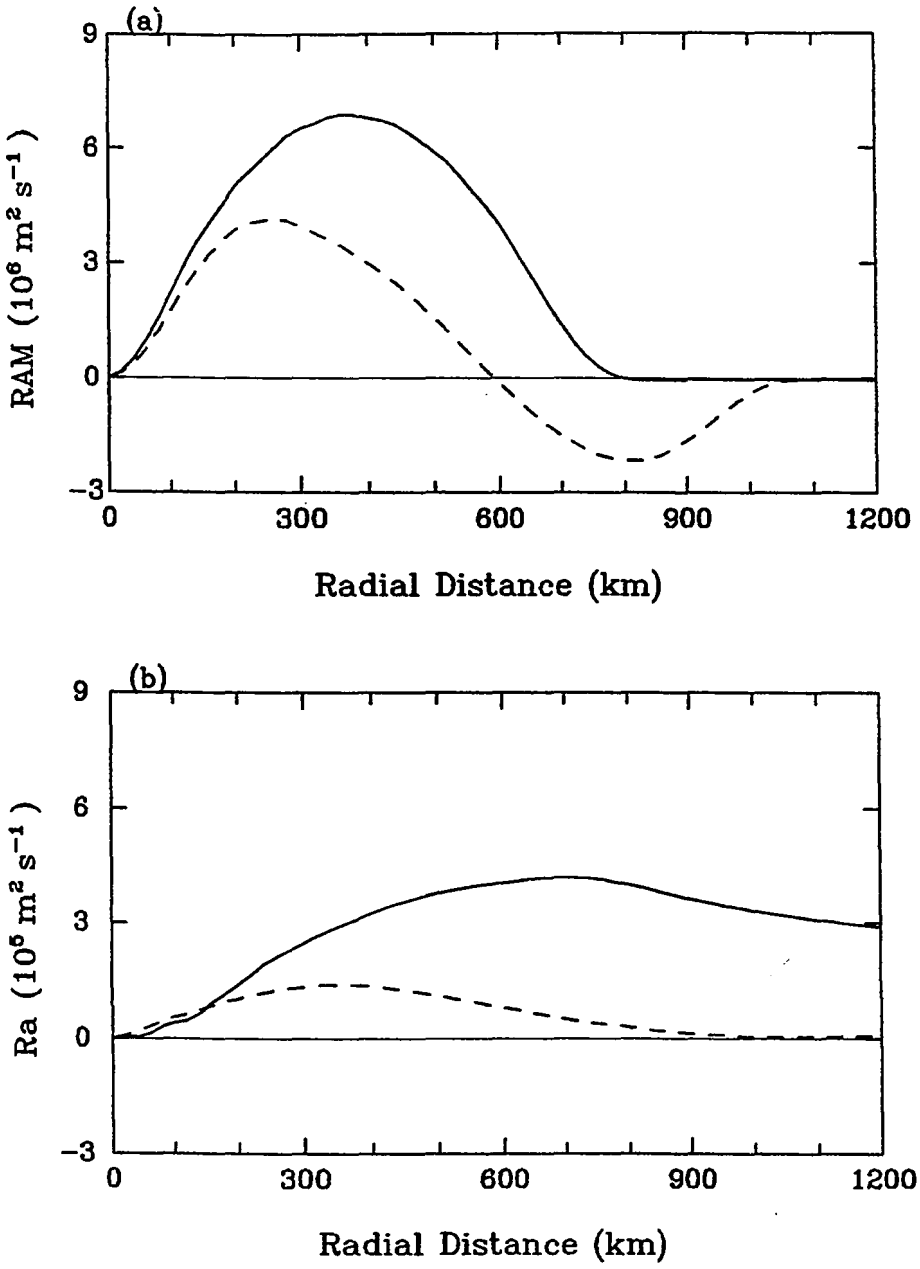

Fig. 6 The radial distributions of (a) relative angular momentum (10^6 m^{2}s^{-1}) and (b) amplitude of the beta-gyres (10^5m^{2}s^{-1}) at 625 mb at hour 6. Solid and dashed lines are for case S and case W, respectively.

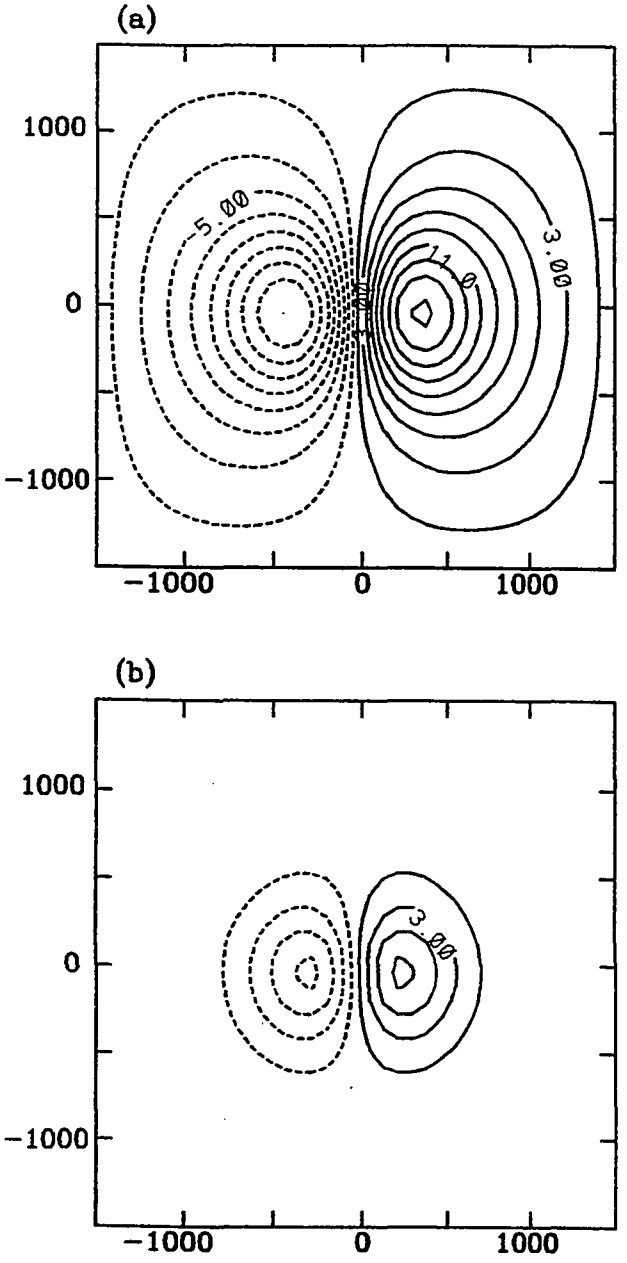

Fig. 7 The Streamfunctions of initial asymmetric circulations at 625 mb with a contour interval of 2×10^3 m^2s^{-1} for (a) case S and (b) case W. Abscissa and ordinate units are km.

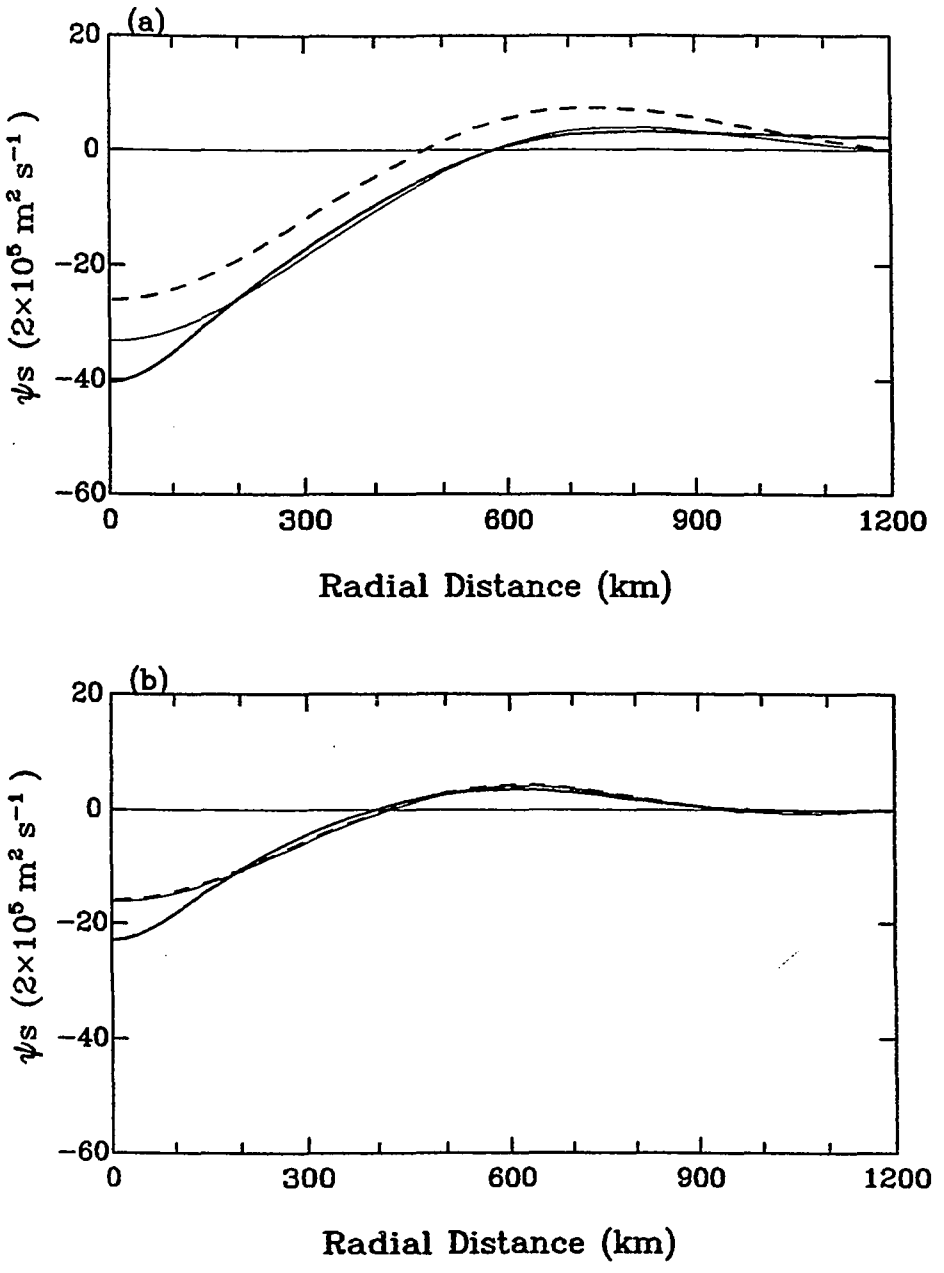

Fig. 8 The sum of the first three radial modes of symmetric circulation (thin solid lines) at 625 mb at hour 24 for (a) case S and (b) case W. Thick solid lines denote total symmetric circulation, and the dashed lines present the sum of the second and third radial modes.

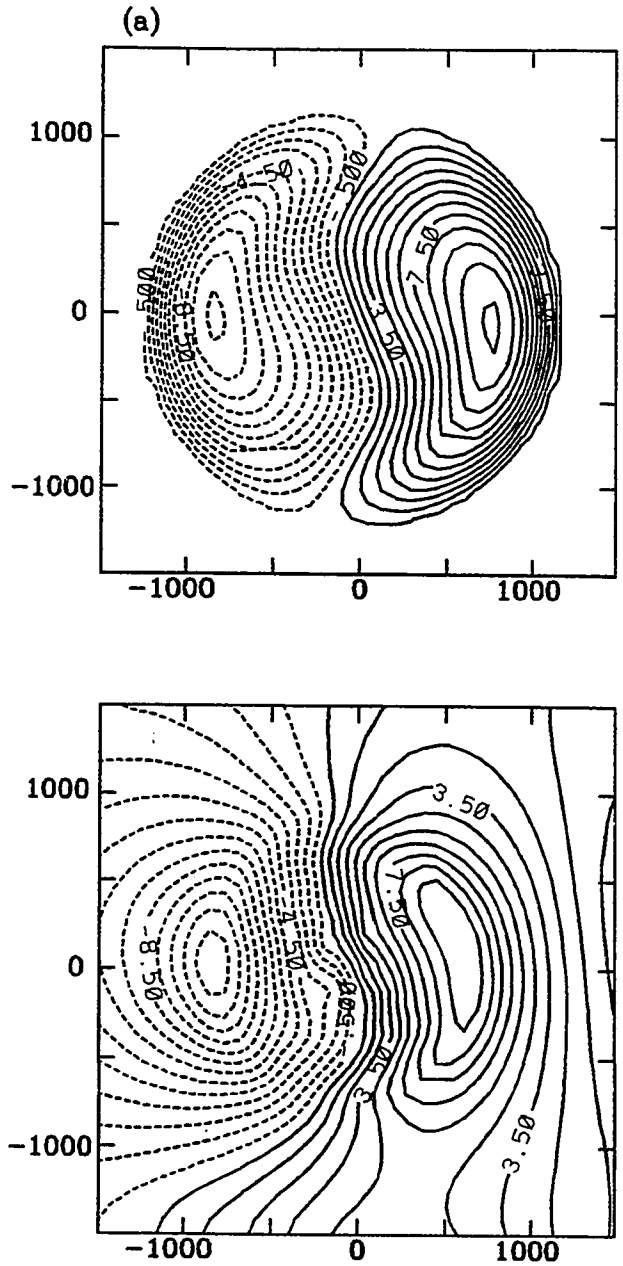

Fig. 9 The sum of the first three radial modes of asymmetric circulation (upper panel) and the total asymmetric circulation (lower panel) at 625 mb at hour 24 for (a) case S and (b) case W. Abscissa and ordinate units are km. Contour interval is 10^5 m^2s^{-1}.

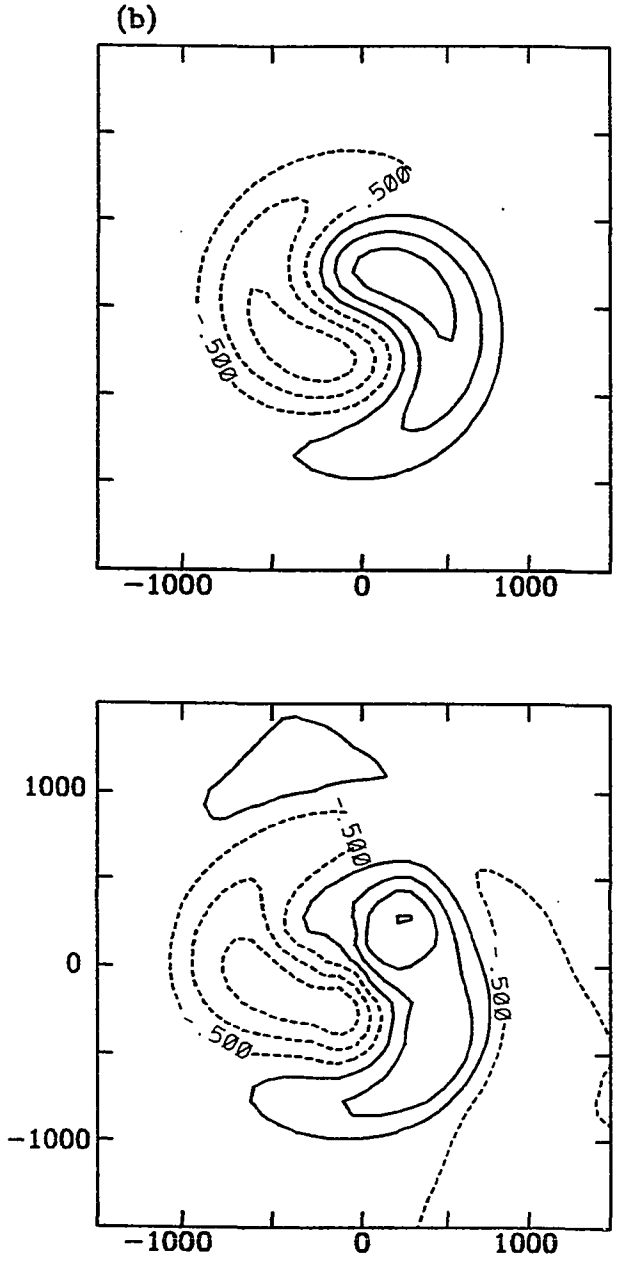

Fig. 9 Continued.

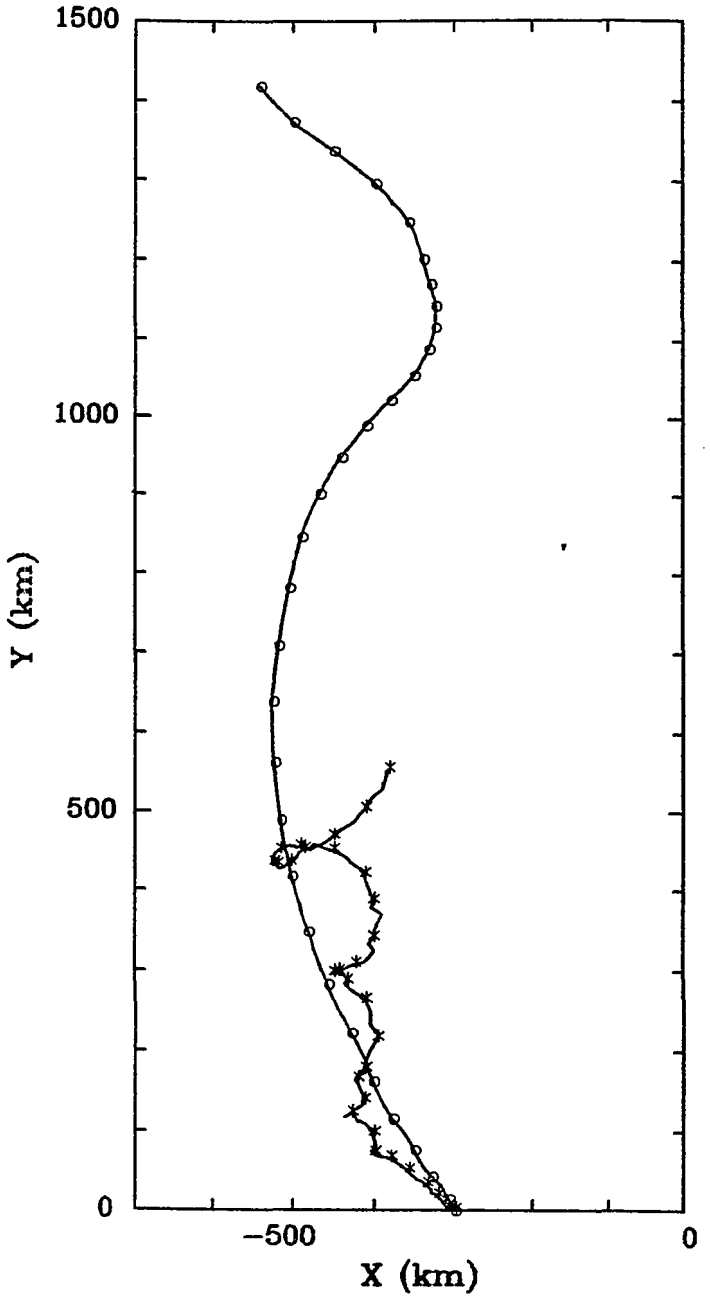

Fig. 10 Vortex tracks at 6-hour interval for case S (O) and case W (*) during 180-hour integrations using a shallow-water model. Abscissa and ordinate units are km.

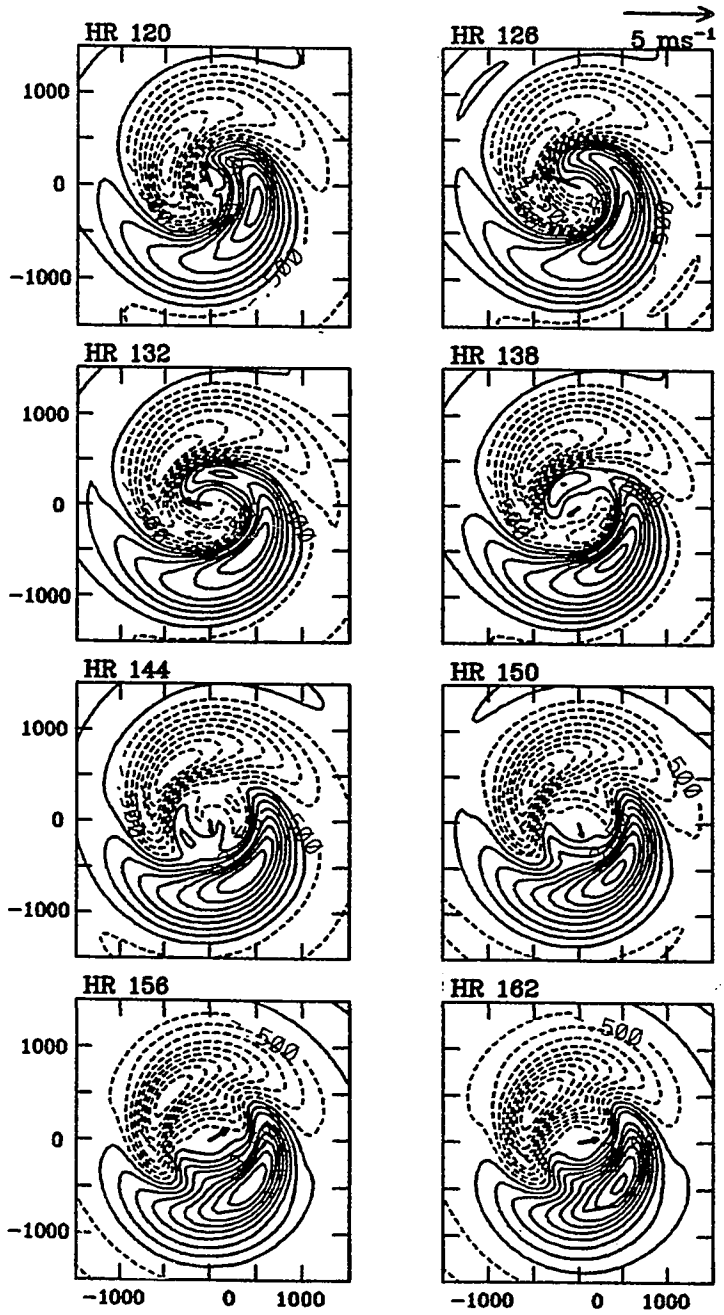

Fig. 11 The streamfunctions of the beta-gyres for case W from hour 120 to hour 162 with a contour interval of $10^5 m^2 s^{-1}$. The arrow at the vortex center denotes the drifting velocity of the vortex. Abscissa and ordinate units are km.

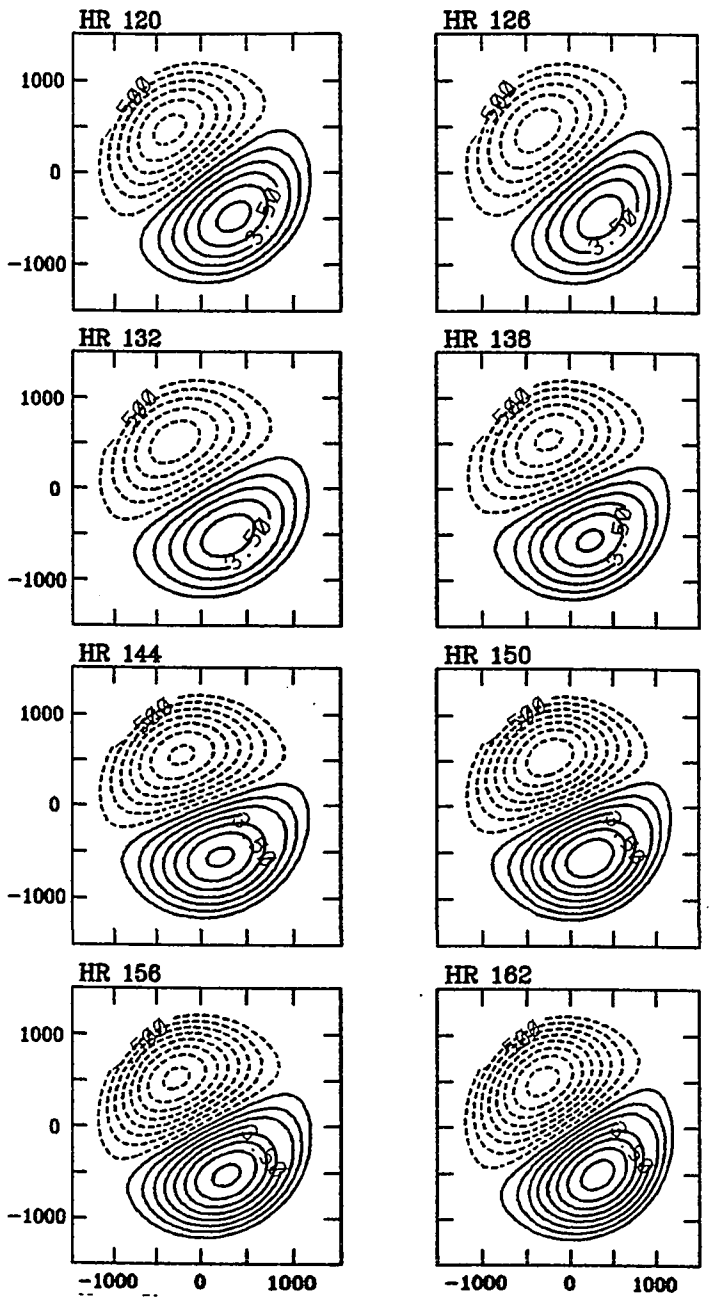

Fig. 12 As in Fig. 11 except for the first radial mode of the beta-gyres.

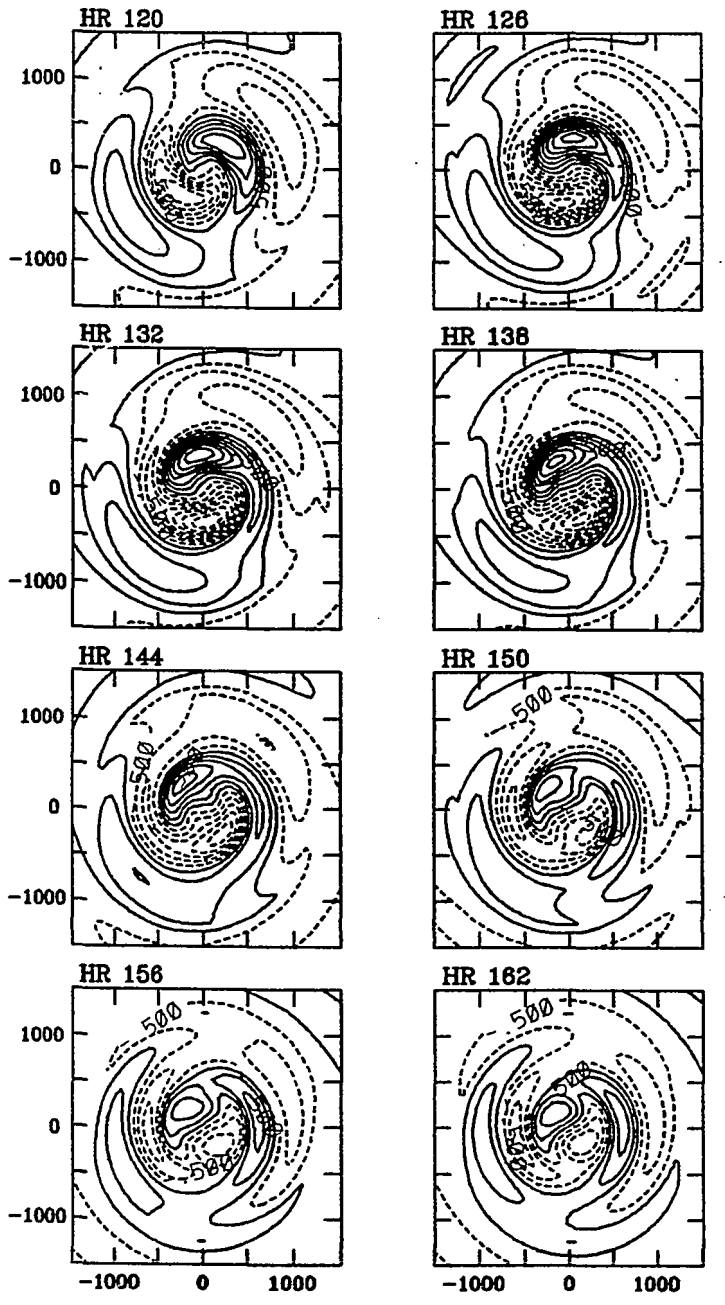

Fig. 13 As in Fig. 11 except for the residual of the beta-gyres.

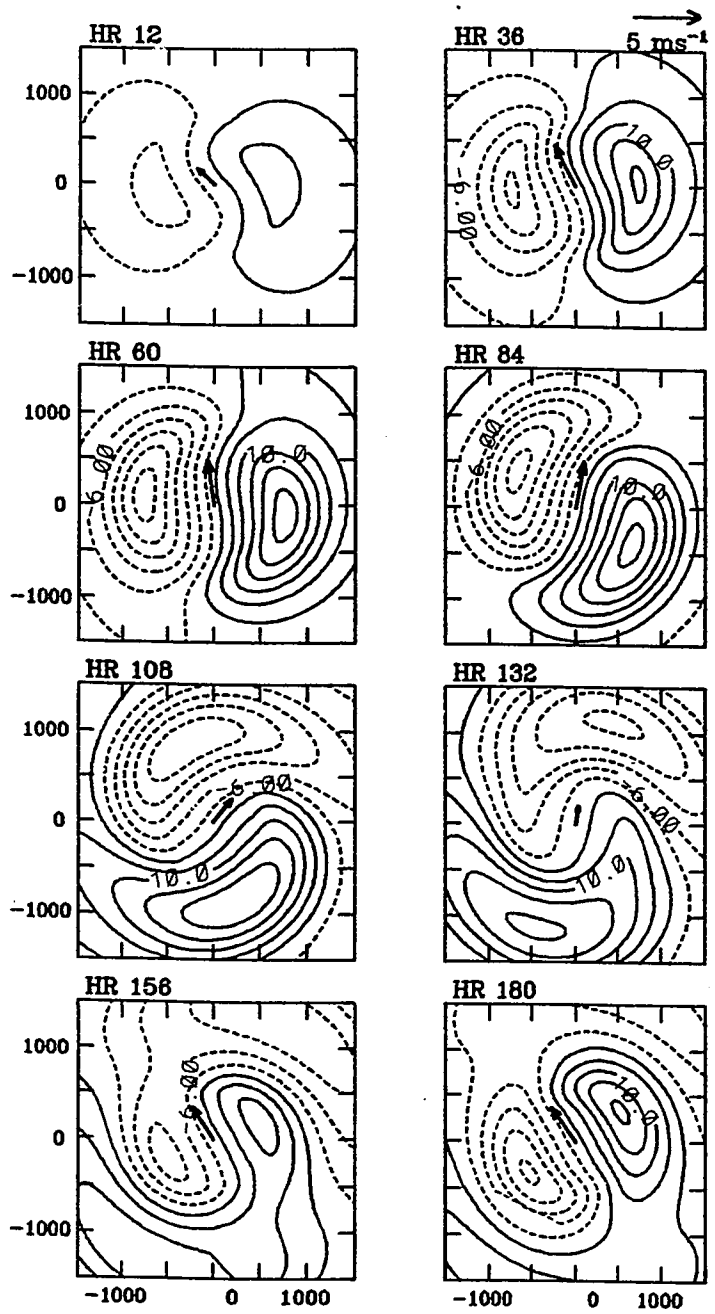

Fig. 14 The streamfunctions of the beta-gyres at every 12 hour with a contour interval of 4×10^5 m^2s^{-1} for case S during a 180-hour integration. The arrow over the vortex center denotes the drifting velocity of the vortex. Abscissa and ordinate units are km.

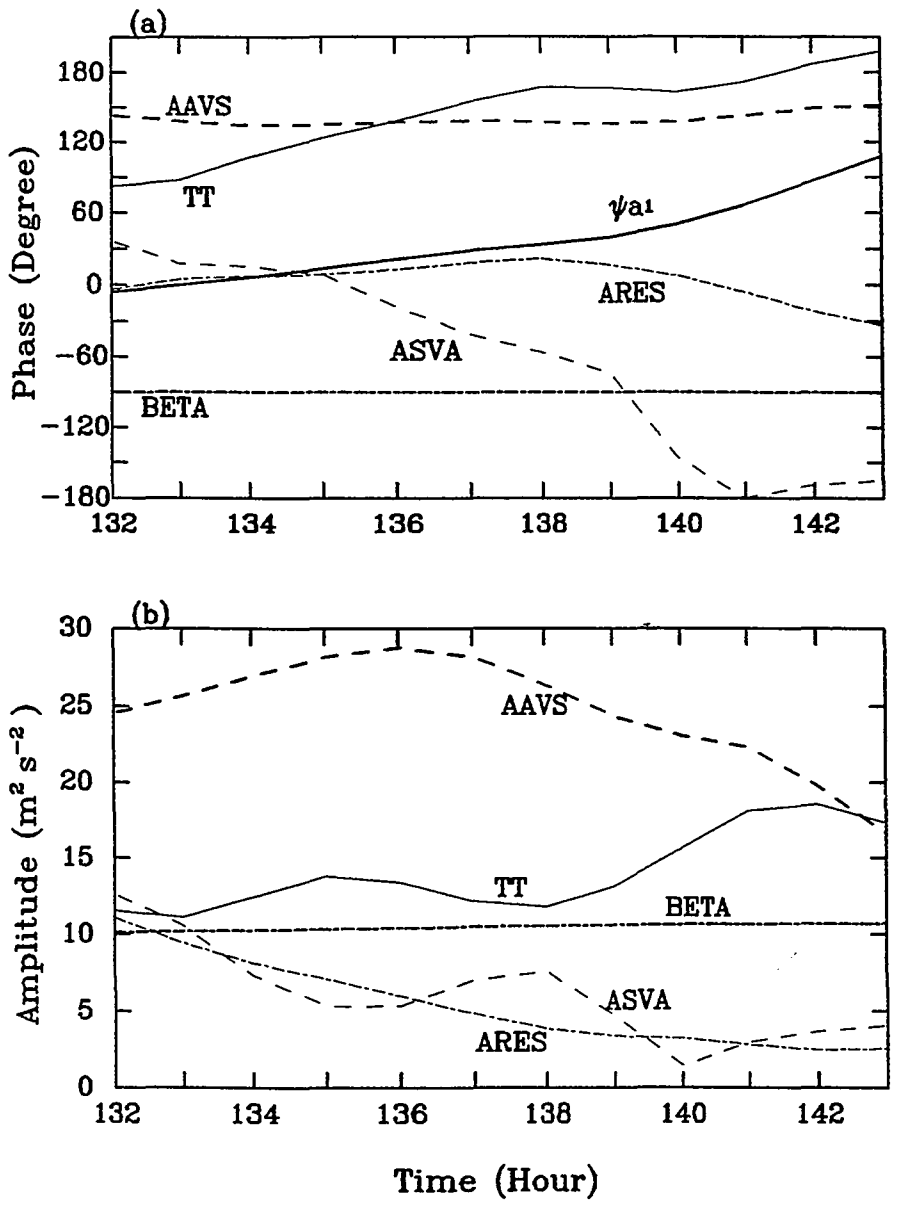

Fig. 15 (a) The phase (degree) and (b) the amplitude (m^2s^{-2}) of the terms TT, AAVS, ASVA, BETA and ARES at 300 km radius from hour 132 to hour 143 in case W. Thick solid line in (a) denotes the phase of the beta-gyres. See Eq. (3.19) for the meaning of abbreviations.

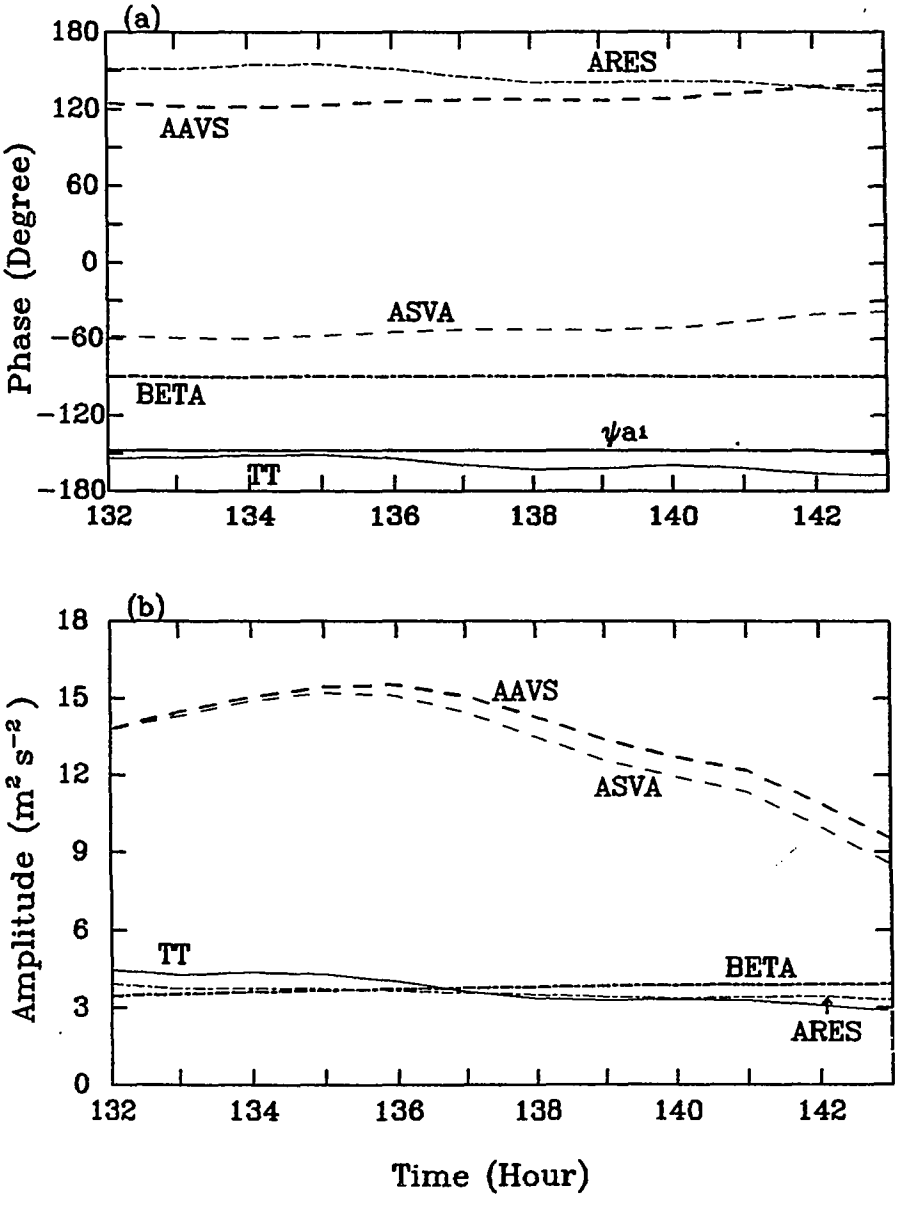

Fig. 16 As in Fig. 15 except at 600 km radius.

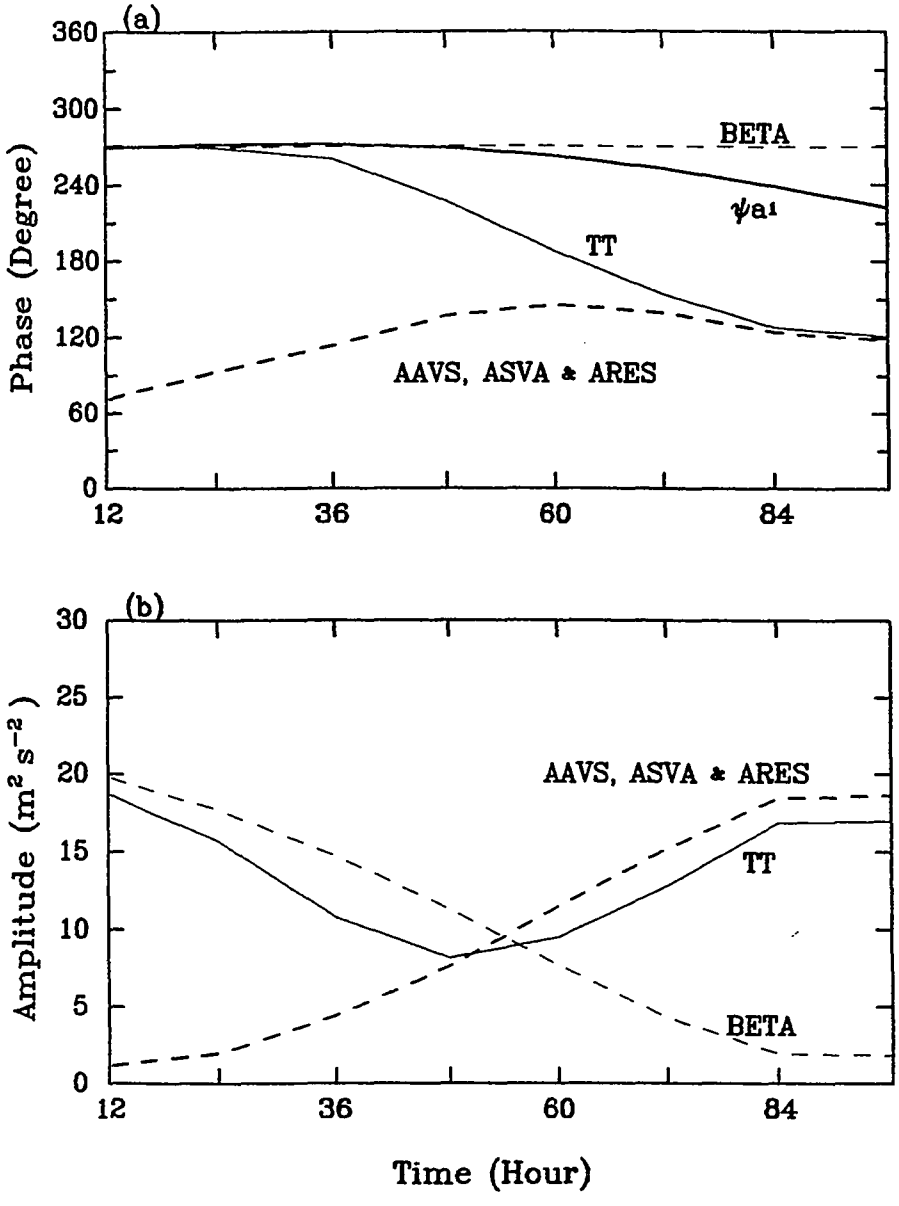

Fig. 17 (a) The phase (degree) and (b) the amplitude (m^2s^{-2}) of the terms TT, BETA and the sum of AAVS, ASVA and ARES at 700 km radius from hour 12 to hour 96 in case S. Thick solid line in (a) denotes the phase of the beta-gyres. See Eq. (3.19) for the meaning of abbreviations.

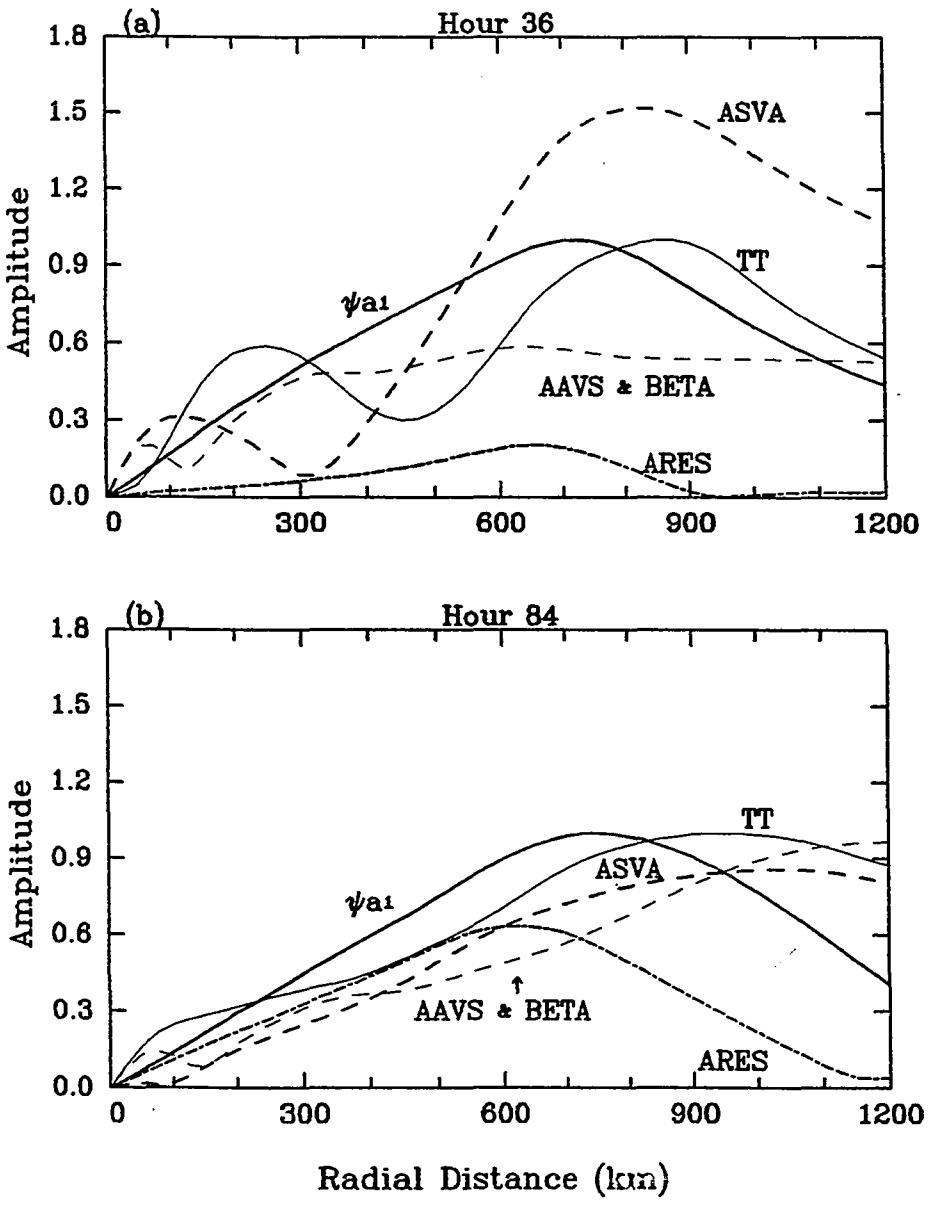

Fig. 18 Amplitudes of beta-gyres (normalized by its maximum), the terms TT, AAVS, ASVA, ARES and and the sum of AAVS and BETA (divided by the TT maximum) as functions of radial distance (km) in case S at (a) hour 36, (b) hour 84. See (3.19) for the meaning of abbreviations.

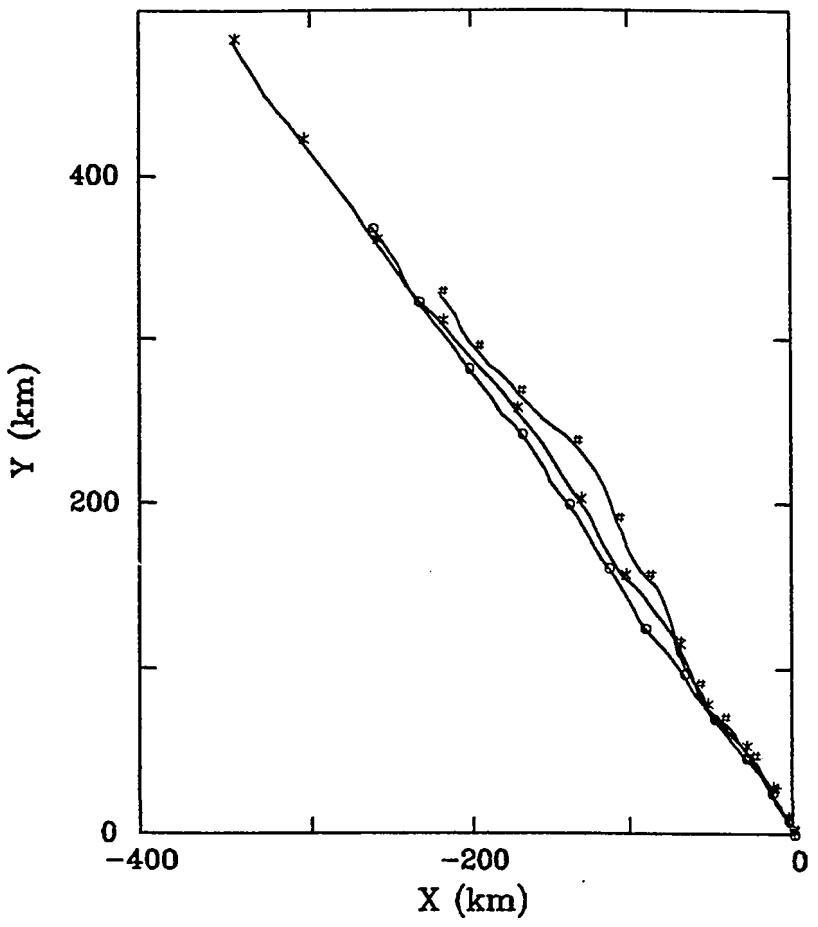

Fig. 19 The propagation tracks of the vortices at 6-hour interval for the constant anticyclonic-shear case C_1 (*), the case with no environmental flow C_o (O), and the constant cyclonic-shear case C_2 (#). Abscissa and ordinate units are km.

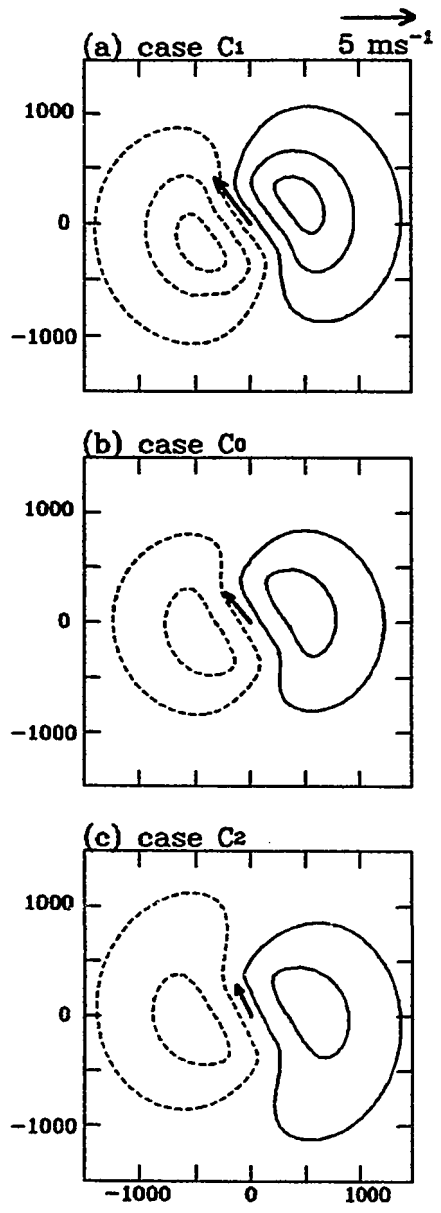

Fig. 20 The streamfunctions of the gyres at hour 48 with a contour interval of 4×10 m^2s^{-1} for (a) case C_1, (b) case C_o and (c) case C_2. Abscissa and ordinate units are km.

Kinetic Energy Budgets at Hour 48

(unit of energy: 10^{12} m^4s^{-2}, unit of energy conversion: 10^7 m^4s^{-3})

(a) case C_1

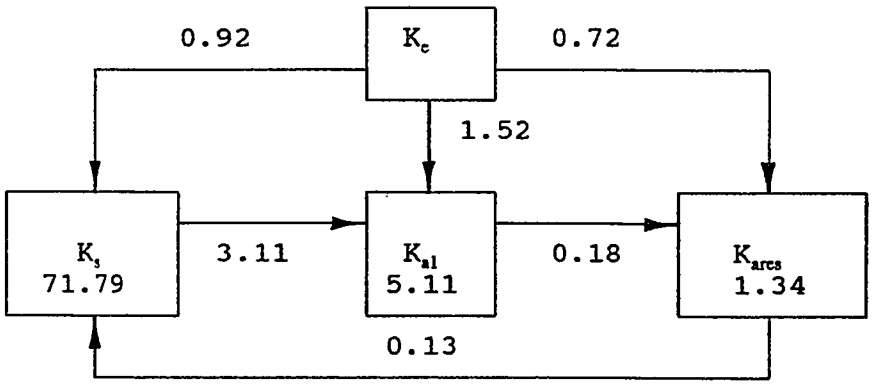

(b) case C_0

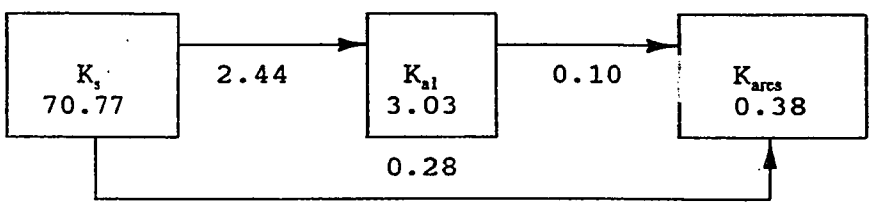

(c) case C_2

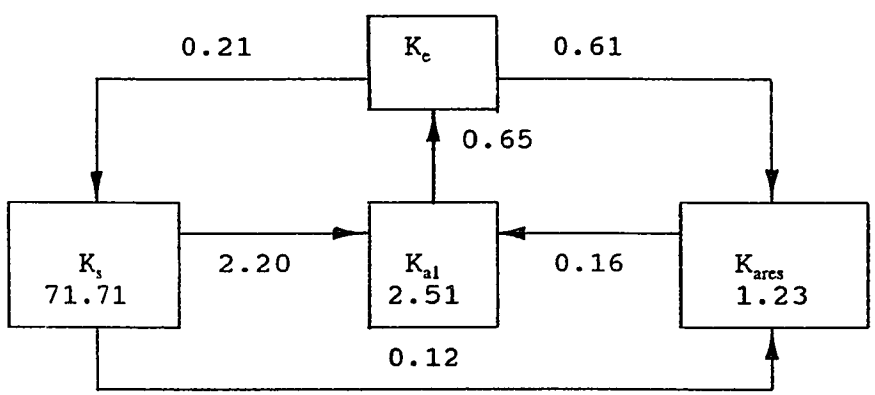

Fig. 21 Kinetic energy budgets at hour 48 for (a) case C_0, (b) case C_1 and (c) case C_2. The values in boxes denote the energy (10^{12} m^4s^{-2}), and the other values represent the energy conversions (10^7 m^4s^{-3}), and the arrows indicate direction of energy transfer.

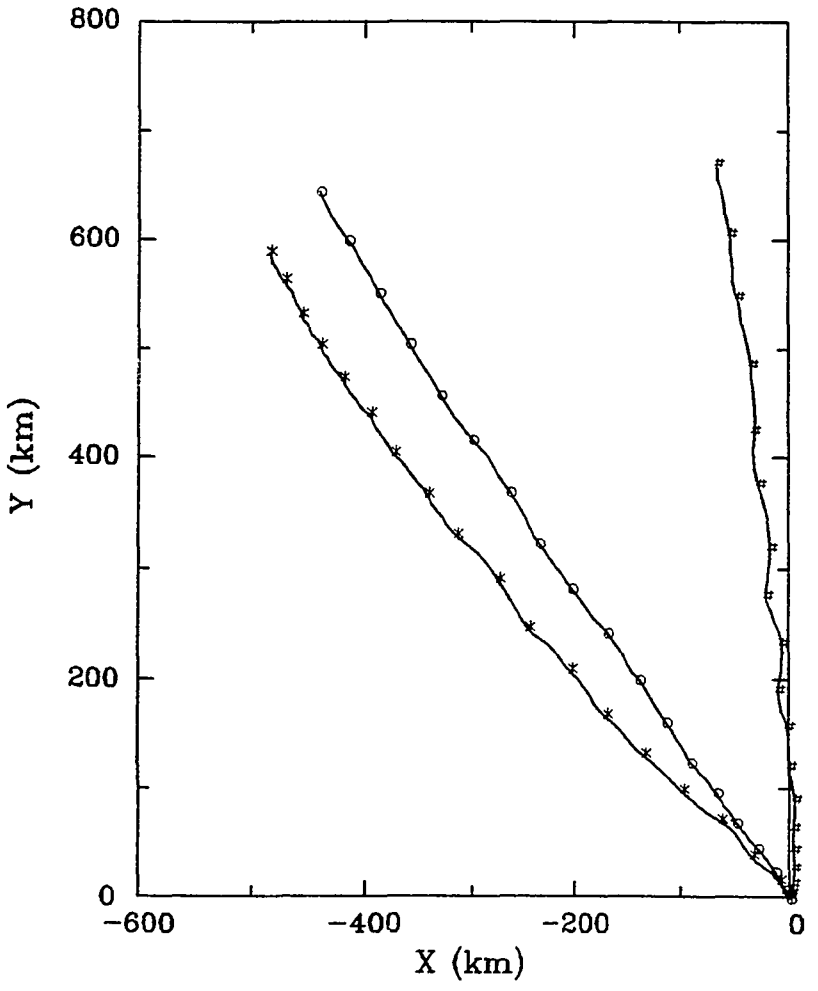

Fig. 22 The propagation tracks of the vortices at 6-hour interval for case D_1 (#), case C_o (O) and case D_2 (*). Abscissa and ordinate units are km.

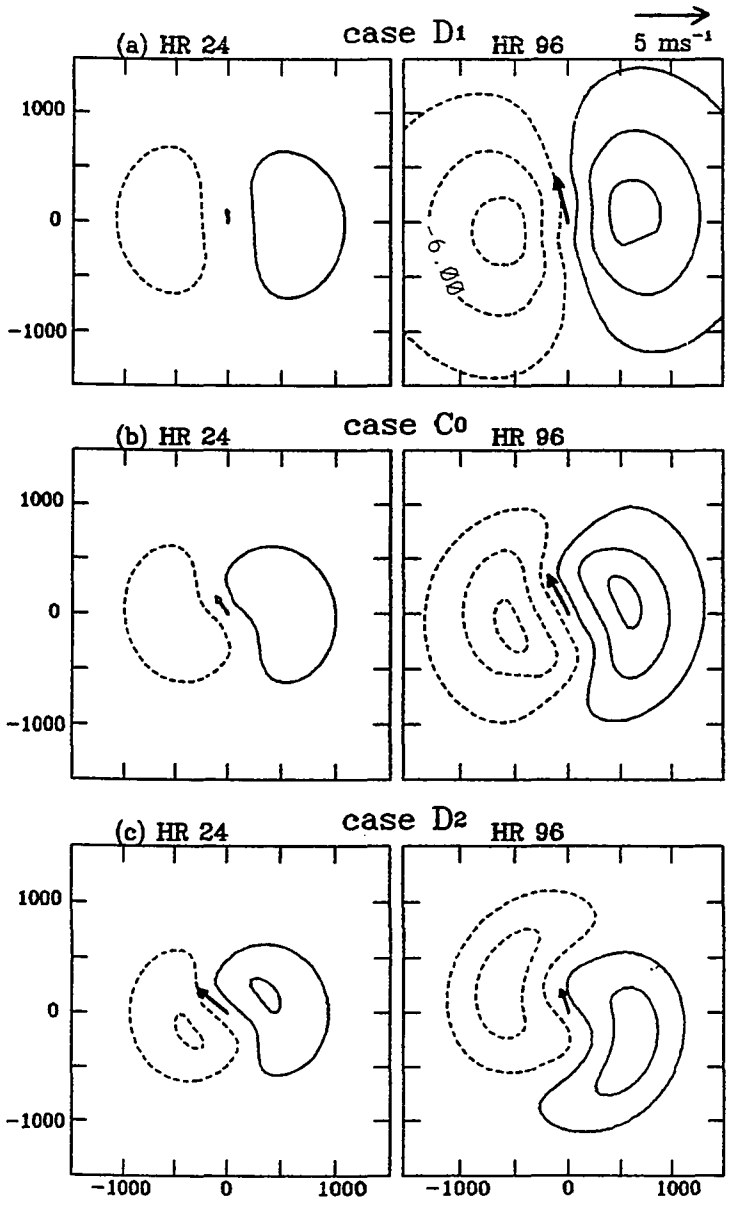

Fig. 23 The streamfunctions of beta-gyres at hour 24 and hour 96 with a contour interval of 4×10 m^2s^{-1} for (a) case D_1, (b) case C_o and (c) case D_2. Abscissa and ordinate units are km.

Kinetic Energy Budgets at Hour 24

(unit of energy: $10^{12}m^4s^{-2}$, unit of energy conversion: $10^7m^4s^{-3}$)

(a) case D_1

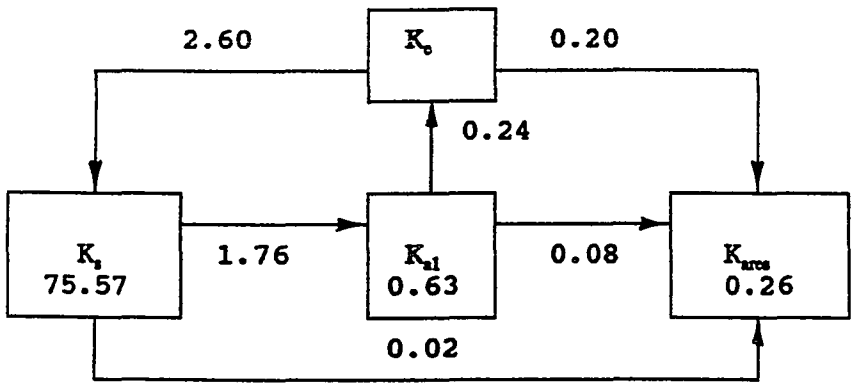

(b) case C_o

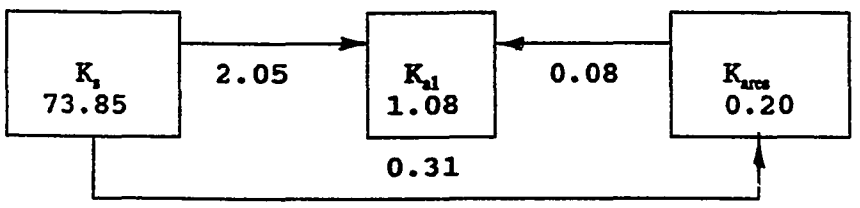

(c) case D_2

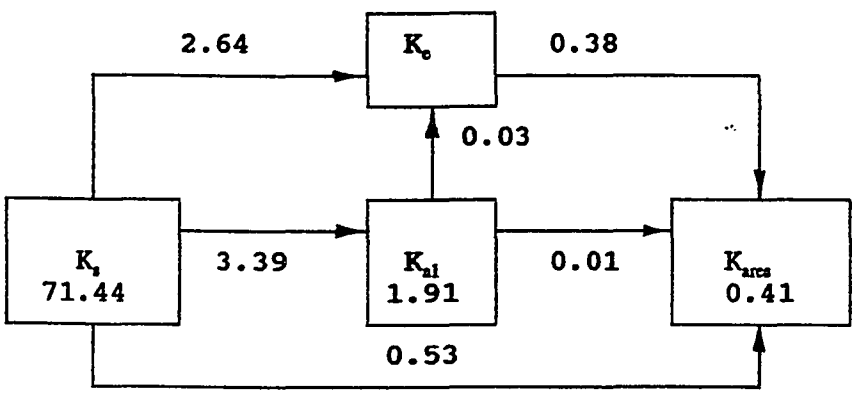

Fig. 24 Kinetic energy budgets at hour 24 for (a) case D_1, (b) case C_o and (c) case D_2. The values in boxes denote the energy (10^{12} m^4s^{-2}), and the other values represent the energy conversions ($10^7m^4s^{-3}$), and the arrows indicate direction of energy transfer.

Kinetic Energy Budgets at Hour 96

(unit of energy: $10^{12}m^4s^{-2}$, unit of energy conversion: $10^7m^4s^{-3}$)

(a) case D_1

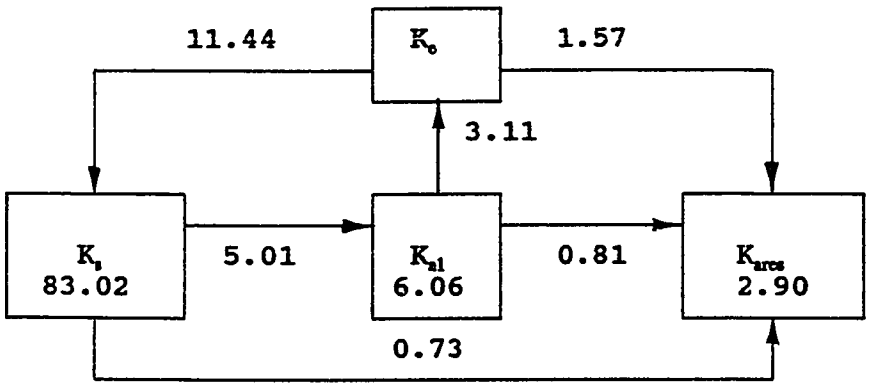

(b) case C_o

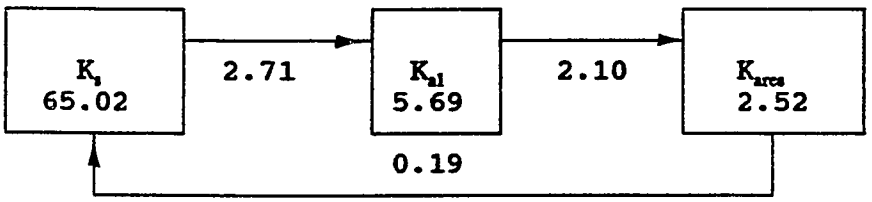

(c) case D_2

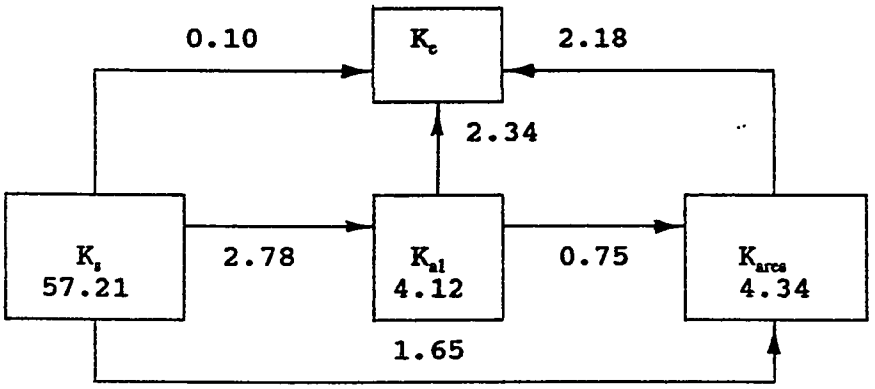

Fig. 25 As in Fig. 24 except at hour 96.

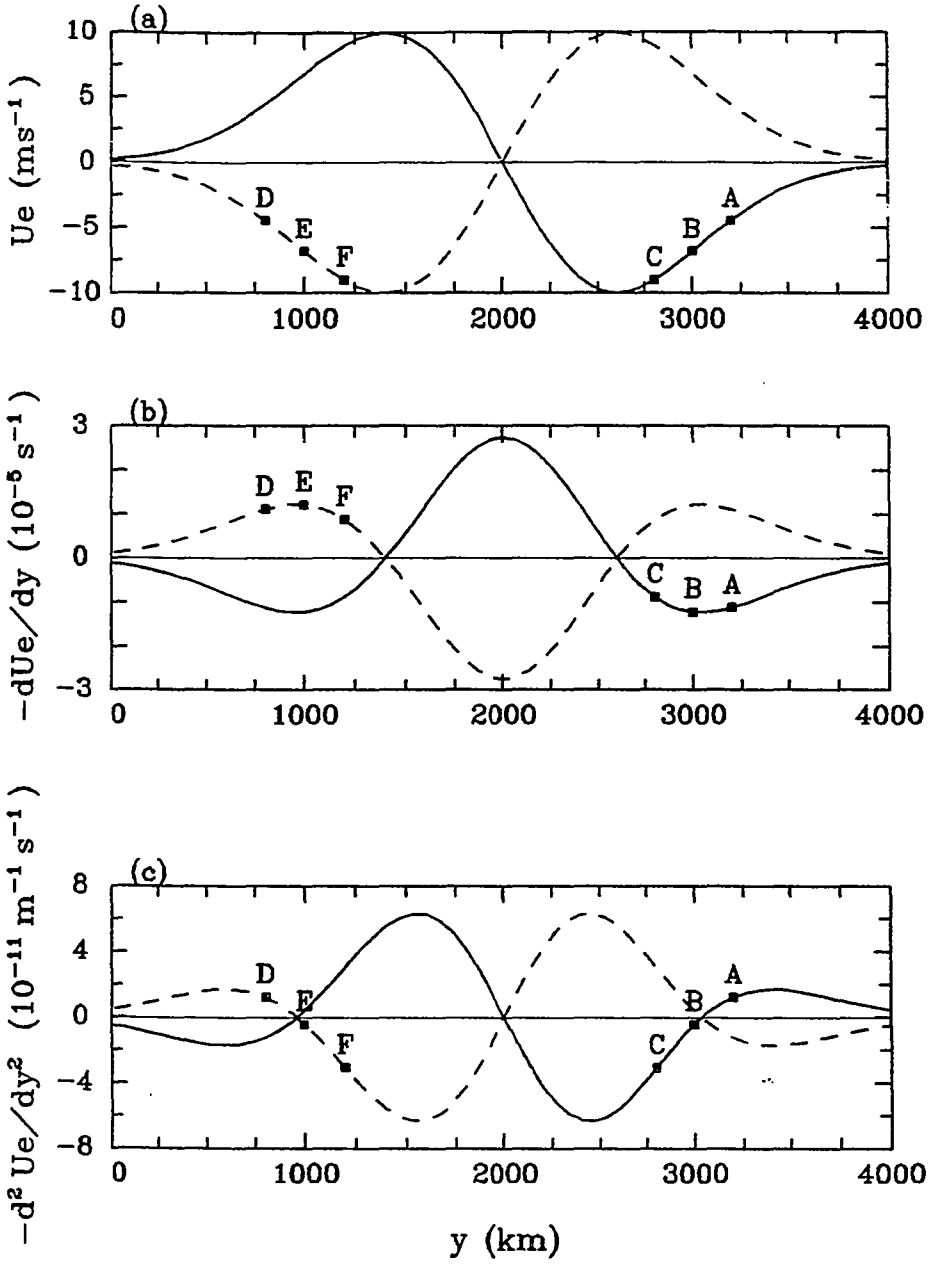

Fig. 26 (a) The zonal wind profile (ms^{-1}) defined by Eq. (4.16) and (b) the corresponding relative vorticity (10^{-5} s^{-1}), and (c) relative vorticity gradient (10^{-11} $m^{-1}s^{-1}$). u_m=-10 ms^{-1} in solid lines whereas u_m=10 ms^{-1} in dashed lines.

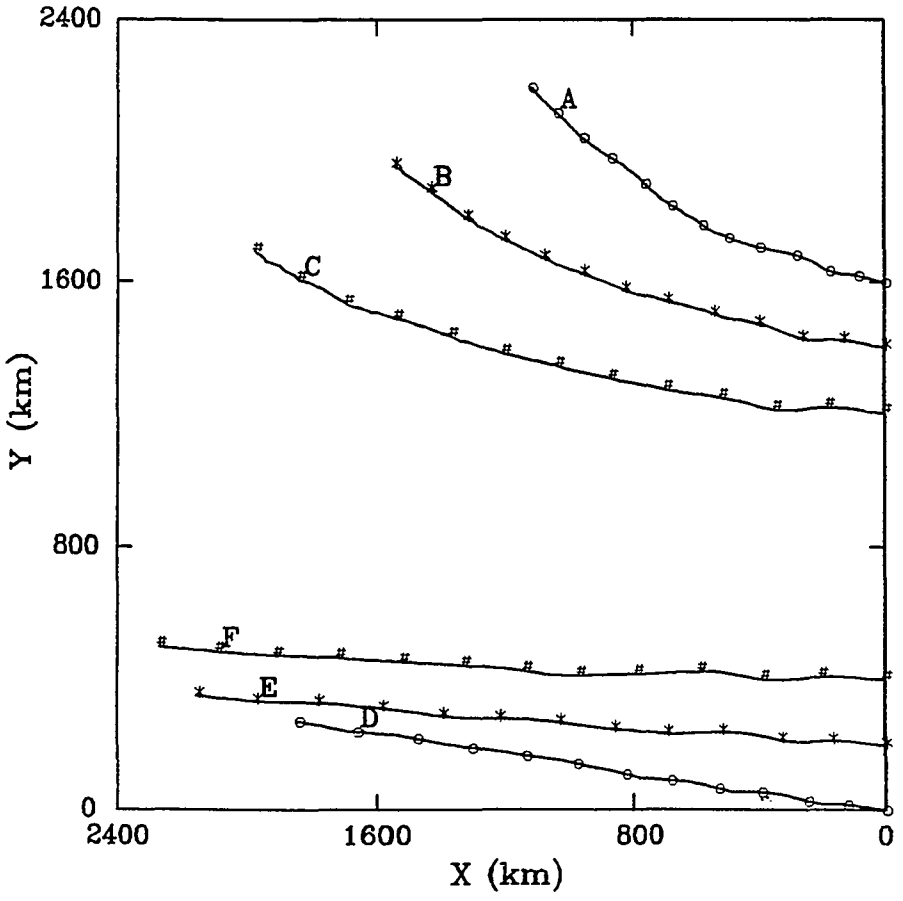

Fig. 27 The track of vortex placed at positions A-F at 6-hour interval. Abscissa and ordinate units are km.

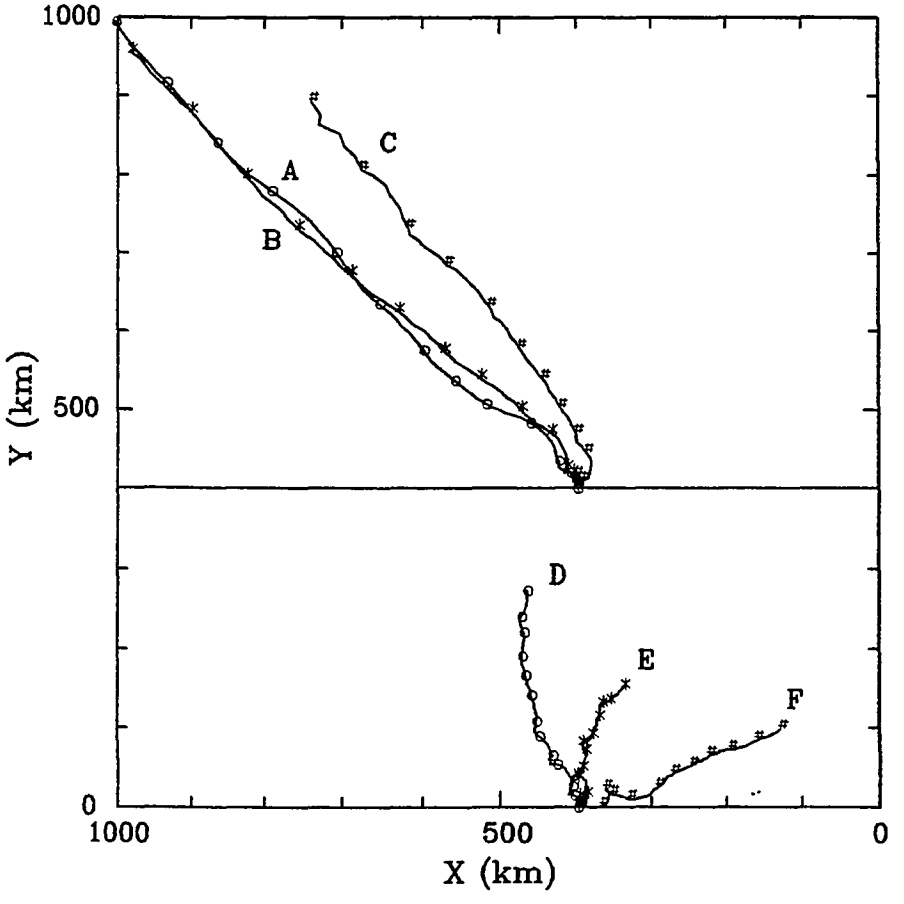

Fig. 28 As in Fig. 27 except for the propagation track.

REFERENCES

Adem, J., 1956: A series solution for the barotropic vorticity equation and its application in the study of atmospheric vortices. Tellus, **8**, 364-372.

Adem, J. and P. Lezama, 1960: On the motion of a cyclone embedded in a uniform flow. Tellus, **12**, 255-258.

Arakawa, A., and V. R. Lamb, 1976: Computational design of the basic dynamic processes of the UCLA general circulation model. Methods in Computational Physics, **17**, 174-264.

Carr III, L. E., 1989: Barotropic vortex adjustment to asymmetric forcing with application to tropical cyclone motion., Ph.D. Dissertation, Naval Postgraduate School, 143pp.

_____, and R. T. Williams, 1989: Barotropic vortex stability to perturbations from axisymmetry. J. Atmos. Sci., **46**, 3177-3191.

_____, and R. L. Elsberry, 1990: Observational evidence for predictions of tropical cyclone propagation relative to environmental steering. J. Atmos. Sci., **47**, 542-546.

Chan, J. C.-L., and W. M. Gray, 1982: Tropical cyclone movement and surrounding flow relationship. Mon. Wea. Rev., **110**, 1354-1374.

_____, and R. T. Williams, 1987: Analytical and

numerical studies of the beta-effect in tropical cyclone motion. Part I: Zero mean flow. J. Atmos. Sci., **44**, 1257-1265.

de Boor, C., 1978: A practical guide to splines. Springer Verlag, New York.

DeMaria, M., 1985: Tropical cyclone motion in a nondivergent barotropic model. Mon. Wea. Rev., **113**, 1199-1209.

Elsberry, R. L., 1986: Some issues related to the theory of tropical cyclone motion. Technical Report NPS 62-86-005, Naval Postgraduate School, Monterey, CA93943, 25pp.

Fiorino, M., and R. L. Elsberry, 1989a: Some aspects of vortex structure related to tropical cyclone motion. J. Atmos. Sci., **46**, 975-990.

_____, and _____, 1989b: Contributions to tropical cyclone motion by small, medium and large scales in the initial vortex. Mon. Wea. Rev., **117**, 721-727.

George, J. E., and W. M. Gray, 1976: Tropical cyclone motion and surrounding parameter relationship. J. Appl. Meteor., **15**, 1252-1135.

Holland, G. J., 1983: Tropical cyclone motion: Environmental interaction plus a beta ,effect. J. Atmos. Sci., **40**, 328-342.

_____, and J. L. Evans, 1992: Interactions between a barotropic vortex and an idealized subtropical ridge. Part II: Structure changes. J. Atmos. Sci., **49**, 963-975.

Jones, R. W., 1986: Mature structure and motion of a model

tropical cyclone with latent heating. Mon. Wea. Rev., **114**, 973-990.

Jordan, C. L., 1958: Mean soundings for the west Indies area. J. Meteor., **15**, 91-97.

Kasahara, A., 1957: The numerical prediction of hurricane movement with the barotropic model. J. Meteor., **14**, 386-402.

Krishnamurti, T. N., 1962: Numerical integration of primitive equations by quasi-Lagrangian advective scheme. J. appl. Meteor., **1**, 503-521.

_____, 1969: An experiment in numerical prediction in equatorial latitudes. Quar. J. Roy. Meteor. Soc., **95**, 594-620.

_____, A. Kumar, K. S. Yap, A. P. Dartoor, N. Davison, and J. Sheng, 1990: Performance of high-resolution mesoscale tropical prediction model. Advance in Geophysics, **32**, 133-286.

Li, T. and Y. Zhu, 1991: Analysis and modelling of tropical cyclone motion (I): The axiasymmetric structure and the sudden change of tracks. Science in China, Series B, **34**, 223-233.

McCalpin, J. D., 1988: A quantitative analysis of the dissipation inherent in semi-Lagrangian advection. Mon. Wea. Rev., **116**, 2330-2336.

McWilliams, J. C., and G. R. Flierl, 1979: On the evolution of isolated nonlinear vortices. J. Phys. Oceanogr., **9**, 1155-

1182.

Robert, A. J., Henderson, J., and Turnbull, C., 1972: An implicit time integration scheme for baroclinic models of the atmosphere. Mon. Wea. Rev., **100**, 329-335.

Rossby, C. G., 1948: On displacement and intensity changes of atmospheric vortices. J. Marine Res., **7**,175-196.

Sasaki, Y., 1955: Barotropic forecasting for the displacement of a typhoon. J. Meteor. Soc. Japan, **32**, 1-8.

Shapiro, L. J., 1983: The asymmetric boundary layer flow under a translating hurricane. J. Atmos. Sci., **40**, 1984-1998

_____, 1992: Hurricane vortex motion and evolution in a three-layer model. J. Atmos. Sci., **49**, 140-153.

Smith, R. K., 1991: An analytic theory of tropical-cyclone motion in a barotropic shear flow. Quar. J. Roy. Meteor. Soc., **117**, 685-714.

Ulrich, W., and R. K. Smith, 1991: A numerical study of tropical cyclone motion using a barotropic model. II: Motion in spatially-varying large-scale flows. Quar. J. Roy. Meteor. Soc., **117**, 107-124.

Wang, B., and X. Li, 1992: The beta-drift of three dimensional vortices: A numerical study. Mon. Wea. Rev., **120**, 579-593.

Williams, R. T., and J. C.-L. Chan, 1992: Numerical and analytical studies of the beta-effect in tropical cyclone motion, Part II: Zonal mean flows. Submitted to J. Atmos. Sci..

Willoughby, H. E., 1988: Linear motion of a shallow-water, barotropic vortex. J. Atmos. Sci., **45**, 1906-1928.